Nano Today (2013) 8, 138—167

Available online at www.sciencedirect.com

SciVerse ScienceDirect

journal homepage: www.elsevier.com/locate/nanotoday

REVIEW

# DNA-directed self-assembly and optical properties of discrete 1D, 2D and 3D plasmonic structures

Steven J. Barrow[a], Alison M. Funston[b,*], Xingzhan Wei[a], Paul Mulvaney[a,*]

[a] School of Chemistry and Bio21 Institute, University of Melbourne, Victoria 3010, Australia
[b] School of Chemistry, Monash University, Clayton, Victoria 3800, Australia

Received 4 October 2012; received in revised form 7 January 2013; accepted 18 February 2013
Available online 13 April 2013

**KEYWORDS**
Plasmonics;
DNA;
Self-assembly;
Optical spectra;
Resonances;
Superstructures;
Nanocrystals

**Abstract** We review recent progress on the assembly of metal nanocrystals using dithiol and DNA based bifunctional linkers to create discrete plasmonic superstructures. The structures formed include one-dimensional linear arrays, two-dimensional trimers and tetramers as well as stable three-dimensional assemblies built up on a substrate. We outline specific aspects and challenges within the DNA-assembly technique, including control of the desired interparticle spacing. The optical properties of a number of general classes of assemblies are described and the consequences of symmetry-breaking, such as the formation of Fano-like resonances. The assembly and optical properties of unique three-dimensional structures are described along with a hybrid top-down and bottom-up technique for obtaining long, linear arrays of crystalline metal nanoparticles.


## Introduction

The growth, assembly and organization of nanoscale particles into superstructures is an interesting scientific challenge for several reasons. Firstly, the chemical fabrication of organized structures is an essential prerequisite for understanding how complexity arises in living systems. Nanocrystal superstructures provide an elegant model system for such studies because the degree of order or disorder in a given artificially assembled system of particles can be quantified by electron microscopy, X-ray scattering and other structural techniques. A second aspect driving research in this direction is related to the harnessing and control of light at the nanoscale. At the present time, it is not possible to assemble nanostructures that can absorb light and vectorially channel the energy in particular directions. It is likely that energy harvesting, storage, transmission and dissipation will be better understood if we can demonstrate how interactions of radiation with nanocrystal superstructures might be harnessed. Finally, these new and complex, composite materials may exhibit unusual optical properties, which lend themselves to applications. In this review we focus on the assembly of gold and silver nanocrystals. This field has gathered momentum because there is compelling evidence and

* Corresponding authors.
*E-mail addresses:* alison.funston@monash.edu (A.M. Funston), mulvaney@unimelb.edu.au (P. Mulvaney).

1748-0132/$ — see front matter © 2013 Elsevier Ltd. All rights reserved.
http://dx.doi.org/10.1016/j.nantod.2013.02.005

data demonstrating useful applications in surface enhanced Raman spectroscopy [1,2], plasmon-enhanced fluorescence [3], amplification of nonlinear optical signals [4], nanoscale lasers [5], plasmon-assisted photolithography [6], plasmon-enhanced solar light harvesting and photocatalysis [7,8], ultrasensitive chemical and biological sensors [9–13], optical circuitry [14,15], logic gates [16] and metamaterials [17–19].

We summarize current progress in (i) assembling discrete artificial nanocrystal structures using DNA linkers and (ii) measuring and predicting their optical properties using the hybridization approach to plasmonic coupling. We discuss a number of different linker-based assembly methods, with a focus on the use of DNA linkers which give enough flexibility to design assemblies of different geometry. We present data for the assembly of two particles and discuss some general limitations and comments on the interparticle separations achieved within assemblies compared to those predicted by the length of the DNA oligonucleotides used. Following these sections we briefly consider plasmon resonances in small particles (this topic is covered in great detail in numerous textbooks [20,21]), and then review relevant concepts for describing the optical properties of coupled nanoparticle systems using as an example the simplest aggregate structure – dimers consisting of two nanospheres. These are then extended to linear arrays of trimers up to hexamers. The linking groups may also be designed to produce predominantly two-dimensional structures such as trimers and tetramers arranged at the vertices of a triangle or square. These assemblies and their optical properties are described in the following section. Along with the formation of higher order structures, a general lowering of the symmetry of the assemblies from the ideal symmetry is observed and discussed. We then give a general approach for the assembly of discrete, highly symmetric, three-dimensional structures on a substrate. Thereafter, we outline the assembly of long, highly uniform, linear arrays using a combination of top-down and bottom-up nanofabrication. Following this, we discuss the formation of chiral structures and larger plasmonic architectures before concluding with future directions for the field.

## Assembly with dithiol based linkers

It has long been known that colloid aggregation typically results in fractal type aggregates [22], regardless of whether that process is diffusion limited or activation controlled. Conversely, it has become possible in the last decade to grow 3D nanocrystal superlattices by slow evaporation of the solvent of surfactant stabilized metal (or semiconductor) nanocrystals (see the review by Prasad et al. [23]). In these colloid-crystals, which may be tens of microns in size and composed of several million individual nanocrystals, the particles typically form an fcc lattice with lattice constants determined by the nature of the adsorbed surfactant layers. Between these two extremes, lies the true challenge in self-assembly and for chemistry as a whole: the controlled chemical assembly of nanocrystals into well-defined superstructures with predictable spatial geometry.

It is with this in mind that the bottom-up assembly of chemically synthesized metal nanocrystals into higher order structures is being actively pursued by a large number of groups as the next step in creating nanostructures for plasmonics. The vast majority of schemes for self-assembly of metal nanoparticles rely on the use of thiol-functionalized linking molecules. Alkanethiols have a strong affinity for gold surfaces [24,25] and gold colloids [26] while dithiols can act as conjugation molecules bridging two nanocrystals together [27,28]. Self-assembly occurs when these ''linker'' molecules are introduced into a gold nanoparticle solution. By manipulating the concentration of linker molecules present in solution, the length and growth rate of the gold nanosphere chains can be controlled. Many different molecules can be used as linkers in gold nanoparticle assemblies [29]. Dithiols [27,28], aliphatic thiols [30–33], biological compounds [34] and thiolated single strand oligonucleotides [35–43] all make suitable linkers, each with their own advantages and disadvantages.

In addition, thiol linkers that include an acid or base moiety can couple via hydrogen bonding. These linkers are often more soluble in aqueous media, and their coupling can be regulated through pH. Common carboxylic acid functionalized aliphatic thiol linkers that have been explored for self-assembly of gold particles in aqueous solutions include 3-mercaptopropionic acid (MPA), 11-mercaptoundecanoic acid (MUA), 16-mercaptohexadecanoic acid (M16A) and cysteine. Amine functionalized thiols such as cystamine have also been employed as linkers [30–33]. Within these schemes, the thiol groups bind to the gold particles while the assembly of the particles is facilitated via the hydrogen bonding of the carboxylic acid (or amine) endgroups. Lower concentrations of MPA allow the formation of dimers while more concentrated MPA solutions cause longer chains to form [32]. Similar results are obtained for both MPA and MUA. In a continuation of this work, Sethi et al. have demonstrated the dependence of aliphatic thiol gold nanoparticle assembly on pH [30]. In this case, MPA, cysteine and cystamine were used as linker molecules, all of which can exist in a zwitterionic state depending on the ambient pH.

A particular advantage of using thiol-functionalized linkers is their propensity to preferentially bind to the tips of gold nanorods [27,28]. The mechanism of this selectivity is not currently understood; however, the recent discovery that the facets at the tips of gold nanorods grown in the presence of silver ions and the surfactant cetyltrimethylammonium bromide (CTAB) are sparsely packed and are different from the facets of the rest of the rod [44,45] suggests that it relates to the gold atom density on the surface. The preferential tip binding leads to the formation of end-to-end dithiol-linked nanorods [28]. The hydrophilic nature of gold nanorods with CTAB ligands and the hydrophobic nature of the dithiol molecules used requires these assemblies be performed in a 1:4 water–acetonitrile solution. UV analysis of the assemblies reveals a red shift of the longitudinal band due to plasmon coupling of the self assembled rods, supported by TEM images of nanochains, although some disorder that occurs during deposition is apparent [28]. Biological molecules have also been investigated as linkers in

self assembly. Gold nanorods functionalized with thiolated biotin have been assembled in an end-to-end fashion upon the addition of streptavidin, utilizing the strong affinity between these two biological molecules [34]. Many biological sensors based on plasmon coupling of gold nanoparticles have been successfully produced using this technology [11,13,10,12].

## DNA capped nanoparticles

Of the many linker molecules available for the self-assembly of nanoparticles, single strand oligonucleotides are perhaps the most versatile [46–49,35–43]. Many structures can be created using oligonucleotides, including one dimensional nanochains of varying length [49–53] and two dimensional nanostructures [47,54]. DNA linkers to facilitate the formation of three dimensional structures have also been designed [46]. Single strand oligonucleotides are extremely versatile, as different structures can be made using the same experimental procedure, with the oligonucleotide sequence being altered to achieve varying nanostructures. The versatility of single strand nucleotides opens up vast possibilities for research into plasmonic coupling as many new and innovative structures can be fabricated with ease for spectroscopic analysis and DNA directed assembly has essentially overtaken other assembly strategies in recent years [35,55,56,36–43]. Self-assembly via oligonucleotides exploits the sequence programmability of DNA, giving selective molecular recognition ability, along with the relative rigidity of its double-helical form [57].

Perhaps the most basic assembly scheme is that involving single stranded oligonucleotide assembly [41] as shown in Fig. 1(a). In this case, two nanoparticle solutions are functionalized with two different, but complementary, strands of an oligonucleotide via a 5′-thiol group (which has been covalently attached to the oligonucleotide). Hybridization of the complementary DNA strands is the driving force behind the assembly of the nanoparticles. This process can produce chains of gold nanospheres, although careful design of the base pair sequencing along with the inclusion of additional probe sequences also allows assembly of two-dimensional structures such as trimers and tetramers (see Fig. 1(a)), bottom sequence). A slightly different approach is shown in Fig 1(b), where instead of exclusively thiolating the 5′ ends, oligonucleotides with either 5′ or 3′ ends thiolated were used. Assembly in this case can be initiated by introducing an additional, unfunctionalized target oligonucleotide with different sections of its base pair sequence complementary to both of the thiolated (and gold-functionalized) oligonucleotides. No information is given as to which assembly scheme, using only 5′ functionalized or both 5′ and 3′ functionalized oligonucletides, is superior in terms of nanostructure yield and providing reliable interparticle spacings.

Monofunctionalized gold nanoparticles can also be assembled into discrete structures using cyclic DNA templates. Aldaye et al. demonstrated that gold nanoparticles could be monofunctionalized with complementary DNA strands, and that these can then assemble onto free, single-stranded cyclic DNA templates of various geometric shapes, such as triangles and squares (as shown in Fig. 1(b)) [37]. It is important to point out that for these assemblies, some variation in interparticle separation and geometry is obvious from the TEM micrographs. Different nanoparticles could be placed at specific locations within the geometric shapes [38]. This DNA templating technique allows a write/erase technique to be devised, whereby a nanoparticle is removed from a specific site and can be replaced by another [38], as well as 'structural switching' and interconversion between different geometries [38,37]. This was achieved by incorporating loops in the DNA template that can shorten the length of the arms of the template (Fig. 1(b) inset). Although this scheme is highly flexible, it relies on the specialized synthesis of oligonucleotides which include within the base pair sequence small molecules (not natural bases) to generate the bends in the DNA.

Before nanoparticle assemblies are discussed in greater detail, it is necessary to discuss the individual building blocks themselves. Metal colloid particles in water are usually stabilized electrostatically by adsorbed ligands. Electrostatic stabilization is weakened in solutions with high ionic strength, since this reduces the range of the interactions. Studies have shown that citrate stabilized gold surfaces have zeta potentials around −30 mV, and Debye–Huckel theory works well. The van der Waals interactions can be measured by atomic force microscopy between gold surfaces that are neutral and reveal a Hamaker ''constant'' of $2.5 \times 10^{-19}$ J, in good agreement with Lifschitz theory. Gold and silver particles stabilized by citrate and other carboxylic acids slowly aggregate below pH 4 due to the decrease in surface charge as the $pK_a$ of the citrate groups is reached. They are also unstable in solutions of high ionic strength such as 0.1 M NaCl, leading to slow irreversible aggregation. Addition of amine or thiol terminated oligonucleotides leads to exchange of the citrate ions by the nucleic acid strands. The resultant particles exhibit not only a more negative zeta potential due to the high charge density on the nucleic acid bases, but they now resist coagulation in high ionic strength media such as PBS buffer. This is due to the fact that the DNA creates an electrosteric layer, i.e. a surface offering both electrostatic and steric resistance to coagulation. Compression of the charged, rigid chains is entropically and energetically unfavourable. In addition, the contact between oligonucleotide chains on adjacent particles occurs at separations where the van der Waals forces are small enough that they cannot induce squeezing of the DNA.

The DNA coating endows the particles with very useful properties. Gold nanoparticles that are capped with a monolayer of DNA strands are stable in environments of high ionic strength (0.1 M NaCl and higher [35,58]), as well as stable at temperatures up to 80 °C.

The stability at high ionic strength turns out to be essential. At low salt, the charge density on the oligo chains prevents hybridization of DNA and particle assembly. DNA requires high levels of salt to be present for hybridization to occur. Hybridization is reversible with thermal melting of the DNA strands occurring at elevated temperatures [59] and melting also occurs if the ionic strength is lowered

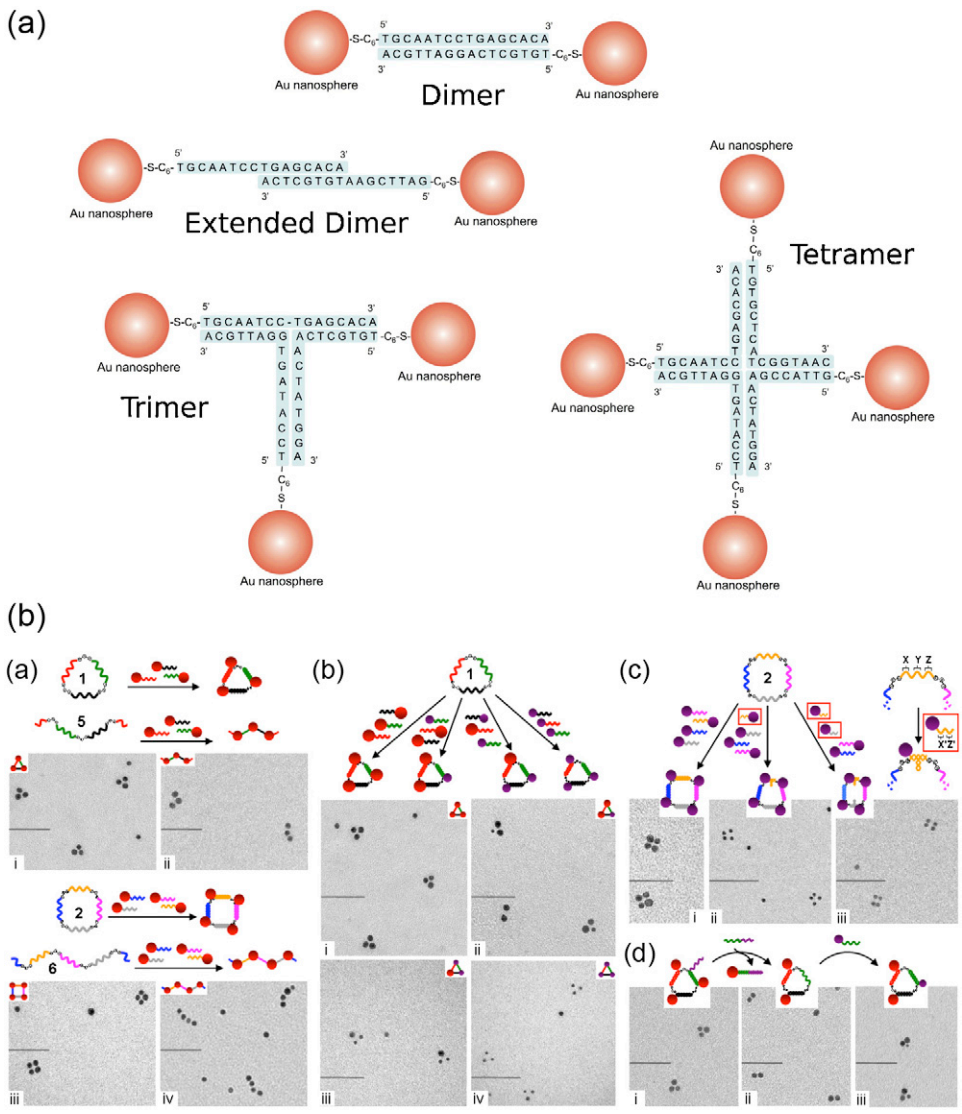


**Figure 1** (a) Assembly scheme reported by Yao et al. [41]. (b) Assembly scheme reported by Aldaye et al. [37] demonstrating the assembly of gold nanoparticles into linear chains, triangles, squares, trapezoids and rectangles. A write/erase function is also shown. Scale bars = 50 nm.

sufficiently. Assembly of nanoparticles via DNA mediated linkers is therefore a reversible process, unlike conventional collapse into the ''primary minimum'' that is assumed to occur in normal particle aggregation. [60]

It is often undesirable to have a monolayer of DNA surrounding nanoparticles, as the availability of more than one DNA strand per nanoparticles will lead to the formation of unwanted assembled byproducts with many different assembly geometries along with the desired structures. To avoid the formation of such structures, it is possible to bind one DNA strand per particle and separate them from multi-strand particles using gel electrophoresis. [48] However, such particles with only one strand do not have the required stability in environments of elevated ionic strength and temperature, when compared to particles with a surface monolayer of DNA. Thus it is necessary to passivate the surface of single strand particles with a stabilizer ligand, such as mercapto-polyethylene glycol molecules. Passivation layers ensure the stability of colloids under the harsh conditions required for DNA hybridization to take place.

## Assembly approaches

Double-stranded DNA motifs adopt a length proportional to the number of base pairs and which is characteristic of the B-DNA double-helix, 3.4 nm per 10 bp. They are also relatively rigid. These factors, along with the recognition of complementary base-pair sequences, endow DNA-based assembly with enormous flexibility. However, superimposed on these benefits are challenges. Assembly involves manipulation of

the double layer forces between the nanoparticles. As such, the ultimate particle spacing is controlled by a balance between the repulsive interactions (due to steric, hydration and electrostatic contributions from the DNA chains) and the van der Waals interactions (primarily between the particle cores). In addition, these may be modified by any capillary drying forces. A fundamental observation from our work, and consistent with other studies, is that the interparticle spacings achieved rarely correspond to molecular models of the ligand chain lengths. Generally, larger particles will squeeze ligand layers more strongly, causing interdigitation of ligand monolayers. Capillary squeezing during drying of nanocrystal structures is also possible. The stabilization afforded by the ligands will depend on the surface coverage and the effective Young's modulus of the ligand layer. Thus, it may be predicted that without consideration of these other factors, DNA self-assembly methods, although useful in controlling the alignment of nanoparticles within a given structure, will not necessarily yield perfect or predictable control of spacing between nanoparticles when the structures are deposited on a substrate [49,41,48,47].

For example, Fan et al. [47] used DNA self-assembly to create gold nanosphere pentamer structures. Particles with diameters of 92.5—74 nm combined with DNA strands containing 95 bp were used in the study, of which the outer 20 bp were complementary and involved in the assembly. Particle spacings of 2 nm were observed, whereas from the length of the DNA strands an interparticle spacing of around 32 nm would be expected. In another study by Sheikholeslami et al., DNA strands consisting of 35 bp were used to create gold—silver nanoparticle dimers with nanoparticle diameters 20—40 nm. Ignoring the length of the functionalized ends, such strands would be expected to give interparticle spacings of approximately 12 nm, however interparticle separations of 3—8 nm were observed [48]. In addition, we have shown in a previous work [49] that the use of particles with large diameters leads to interparticle spacings of approximately 1 nm, even when DNA strands that should yield spacings on the order of 6—8 nm are used. Despite these obvious discrepancies, no systematic investigation into these effects has been reported.

To highlight the effect of van der Waals forces on nanoparticle dimer separation, dimers containing nanospheres of varying sizes (64 nm, 30 nm and 17 nm) were assembled using DNA strands containing 35 bp, which should give a predicted interparticle spacing of 12—14 nm, the results are summarized in Fig. 2. Dimers with an interparticle separation of the order of 1 nm were considered to be in ''primary ligand contact (PLC)'', as this spacing is what is expected for gold particles in the absence of DNA. In other words, if there is insufficient DNA to act as an electrostatic barrier, the interparticle spacing is assumed to be determined by residual citrate groups still on the surface. As van der Waals forces for small particles scale roughly as $R^{-6}$, dimers formed from smaller nanoparticles are more likely to exhibit spacings closer to those corresponding to the hybridized DNA oligomer length. This trend is indeed confirmed in the data shown in Fig. 2. The percentage occurrence of dimers with separations between 12 and 14 nm increases with decreasing nanoparticle size, with 4.7%, 9% and 14% of dimers having an interparticle separation within this range for the 64, 30 and 17 nm particle dimers, respectively. Conversely, dimers in PLC were found for 76%, 59% and 39% of dimers with 64, 30 and 17 nm diameters, respectively. These data suggest that assembly should be performed with small particles, ideally smaller than the 17 nm particles used here, to obtain desired interparticle separations based on the DNA strands used. However, these smaller particles have a much lower scattering cross-section compared to their larger analogues and are difficult to detect with commonly used dark-field microscopes. Another interesting point arising from these data (Fig. 2) is that some dimers have an interparticle spacing larger than that of the fully extended oligonucleotide strand. How such dimers form and remain stable is unclear. Most likely monomeric particles simply adsorb to the glass in close proximity to each other, but the two adjacent particles are not chemically bound to one another.

The use of shorter DNA oligonucleotide linkers, e.g. with just 16 bp, leads to an even lower yield of dimers with the expected interparticle separation (7—9 nm, Fig. S1(a) of the supporting Information), and a larger yield of dimers in deep van der Waals contact. This is consistent with the increase in the van der Waals forces at smaller separations. Although DNA concentration does seem to have some effect on the interparticle separation in nanoparticle dimers, no overriding trend was discerned (see Fig. S1(b) in the supporting information).

These complexities lead to consequences for the investigation of the optical properties of assembled structures. The yield of the desired structure via DNA-based assembly is generally relatively low, making bulk, or ensemble, measurements largely inappropriate. If there is more than one DNA strand attached per particle in an assembly reaction, the assembly will not stop once a desired structure has been assembled. Larger, higher-order by-products will continue to form, with DNA hybridization continuing until all DNA strands have hybridized, resulting eventually in mass aggregation within the colloidal solution. Assembled samples therefore need to be coated onto a substrate in order to 'quench' the assembly reaction. However single particles and higher-order aggregates will still be present. Purification, via agarose gel electrophoresis, can produce functionalized colloidal samples with 1 DNA strand per particle, increasing the yield of the desired nanostructure post assembly [48]. However, dimer yields of only 60—80% percent are achieved using this process. Thus the assembled structures need to be interrogated at the single-particle level, in combination with a technique to determine the exact interparticle separations and geometry of the individual structures.

## Rayleigh scattering spectroscopy of single particles

Much of the spectroscopic data to be discussed in subsequent sections has been gleaned from the study of light scattered by single particles. The light scattered is primarily due to excitation of surface plasmon (SP) resonances. These resonances (formally localized surface plasmon polaritons, LSPP) in small spherical particles in the far-field are calculated from the scattering and absorption cross sections.

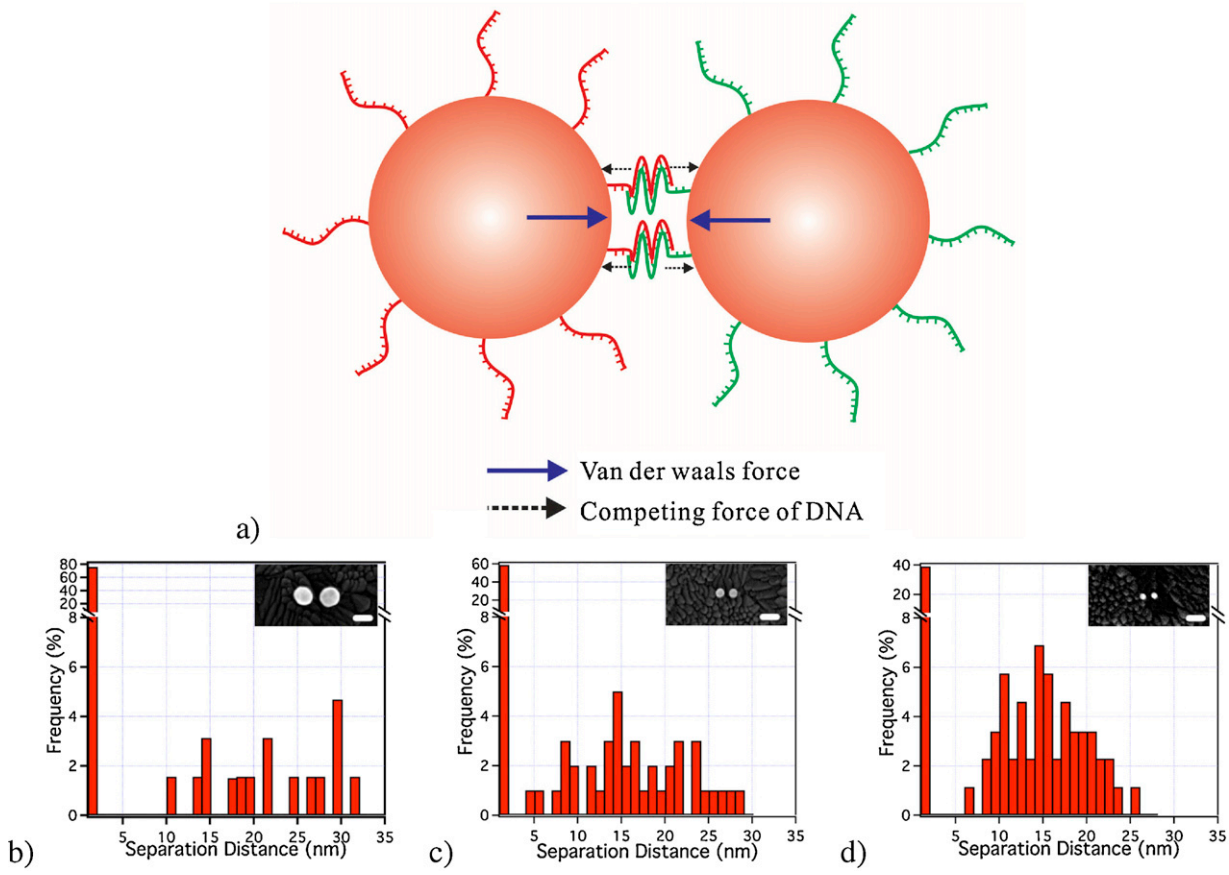


**Figure 2** (a) A schematic of an assembled dimer showing the attracting force of Van der Waals and the repelling force of the hybridized DNA strands. Statistical distributions of the spacings of dimers with gold nanoparticles of 60 nm (b), 30 nm (c) and 17 nm (d) in diameter are shown. 35 base length DNA strands were used in these experiments. Insets show SEM images of dimers with 14 nm interparticle spacings. Scale bars = 50 nm.

These were first determined by Mie (and independently by Debye) and are expressible as a series expansion involving multipoles in terms of Ricatti–Bessel functions. For small enough particles, such that $ka \ll 1$, where $k = 2\pi n/\lambda$, the polarizability of a sphere, $\alpha$ is given by

$$\alpha = 3V\epsilon_m \frac{l(\epsilon - \epsilon_m)}{l\epsilon + (l+1)\epsilon_m} \tag{1}$$

where $\epsilon$ is the dielectric function of the particle, $\epsilon_m$ is the dielectric function of the medium, usually taken to be dispersionless and real, while $l$ is the orbital momentum number of the mode, and takes integral values upwards from $l = 1$, which corresponds to the dipole mode. In the limit of large $l$, the modes tend towards the limiting value of $\epsilon = -\epsilon_m$, the resonance condition for excitation of surface plasmons on a flat film. In reality, this equation fails for larger particles due to retardation, i.e. the exciting radiation field is not uniform across the particles. For very small sizes, the material may exhibit quantum size effects, which modify the dielectric function and these effects can also lead to mode shifts and enhanced damping of resonances [61].

In order to facilitate the investigation of colloidal crystals, spectroscopy techniques have been developed to interrogate a single nanocrystal or assembly. These include near-field techniques (SNOM and EELS) as well as far-field techniques (single crystal extinction, absorption and scattering). Laser-based absorption techniques allow for the investigation of the vibrational dynamics of single particles; however, the complexity of the equipment required for these experiments has not led to their widespread use [62–64]. In contrast, following pioneering work by Feldmann et al. to determine the far-field spectra of individual gold nanoparticles via elastic scattering [65], a number of new techniques based upon the scattering of light by metal particles have been developed. Perhaps the most common of these is dark-field microscopy (DFM), in which the particles are excited using either an evanescent field from totally internally reflected light [66] or a dark-field condenser with central beam block to form a hollow cone of light. The Rayleigh scattering is dependent upon the size and shape of the nanocrystal and scales as the sixth power of the particle diameter (for a sphere); this places a lower practical limit on the size of particles that can be detected using dark field microscopy. Zsigmondy was the first to study the

scattered light from metal nanoparticles using a so-called ultramicroscope. In contrast, absorption techniques are able to measure the optical properties of particles as small as 2.5 nm [62].

While it is an elegant technique, surface plasmon spectroscopy (SPS) of single particles introduces its own challenges. For example, it is not possible to unambiguously determine the size and shape of the actual particle purely by examination of its scattering spectrum. Thus, whilst the plasmon energy, homogeneous linewidth [67,68] and even extinction [69] can be obtained, this cannot be directly correlated to the precise morphology of the individual particles, as the size and shape of the particle giving rise to the spectrum remain unknown. To circumvent this issue, a number of methods have been developed to map and correlate the single particle spectrum (either absorption, extinction or scattering) with its image. Focussed Ion Beams (FIB) can be used to create registration marks for rapid location and re-location of the same nanoparticle [70], and various other correlation schemes have also been reported [71,68,72–75]. Generally high resolution (FEGSEM) imaging does less damage to nanoparticles than TEM, though the latter offers greater resolution [75]. The correlation of the particle's optical spectrum with its morphology has proved to be particularly powerful. It has allowed the retardation of the plasmon resonance to be experimentally determined for a number of particle shapes which were previously inaccessible in ensemble measurements due to the shape and/or size polydispersity of the colloid sample [76,77]. The drastic effects of surface roughness and facet rounding have been demonstrated through single particle studies [76], as well as slight morphology differences [70,77] and the effect of chemical processes such as catalysis, nanocrystal growth and nanocrystal charging on the nanoparticle morphology [78,79].

When two nanoparticles are in close proximity, that is, within 2.5 times the particle diameter of each other, the near-fields of the particles interact, coupling together to generate new optical properties. The coupling of the localized surface plasmon resonance of nanoparticles creates areas of extremely high electromagnetic enhancement for SERS with $|\mathbf{E}|^2$ calculated to be up to $5 \times 10^4$ [80], although recent experimental results have claimed enhancement factors of the order of $10^{10}$–$10^{11}$ [81,82]. Kneipp and colleagues proposed that this enhancement could be exploited through surface enhanced Raman spectroscopy (SERS), as a means to attain single molecule detection [83–85]. Full discussion of the calculation of the optical properties of plasmonic superstructures is given in a number of recent reviews [86,87].

## Dimers

As a consequence of the synthetic challenges already outlined, many researchers initially employed electron beam lithography (EBL) to fabricate nanoparticle arrays, chains and periodically repeating sets of nanoparticles organized as interacting pairs. The absorption/scattering properties of such arrays, containing many interacting nanoparticle structures [88–93], as well as single lithographically fabricated structures from within the array [94] have been investigated. An example of such an array is shown in Fig. 3. The optical characterization of the arrays led to an understanding of coupling within nanoparticle dimers. These experimental investigations have been well-backed up by the theoretical investigation of nanoparticle pairs

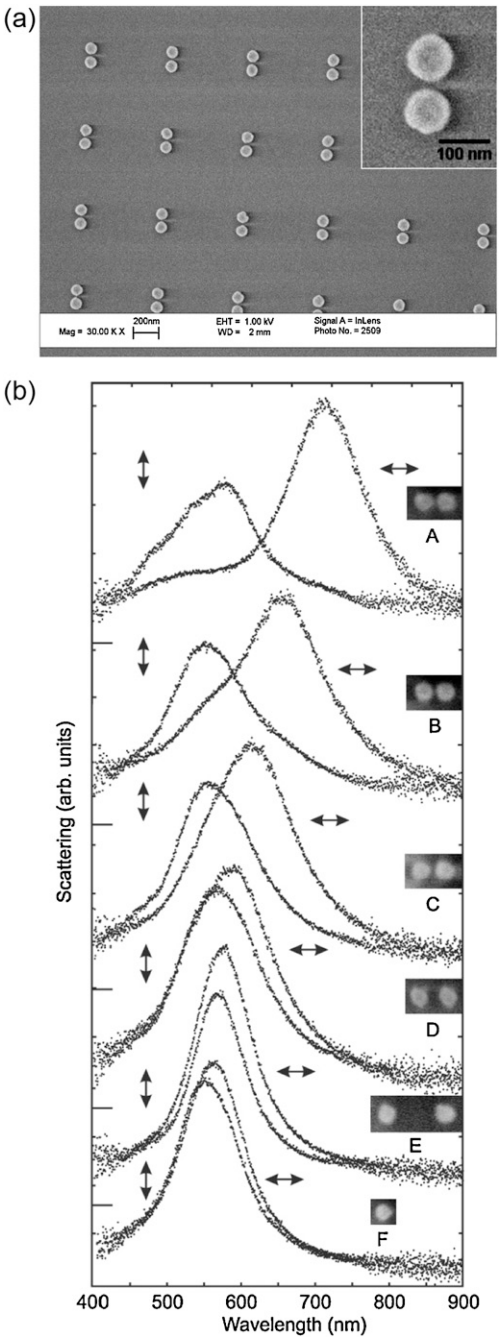


**Figure 3** (a) SEM image of an array of lithographically fabricated nanodisc pairs as reported by Jain et al. [90]. (b) Dark-field spectra and SEM micrographs from isolated particle pairs with varying separation in parallel and perpendicular polarization, as indicated by arrows. The separations (gaps) between the particles are $d \approx$ (A) 10, (B) 15, (C) 25, (D) 50, and (E) 250. Spectrum F from a single particle is included for comparison. From the work of Gunnarsson et al. [94].

via a number of theoretical methods [95—97,80], and some calculations have included particle pairs with less than 2 nm separation [98—101]. However, the resolution limit of modern EBL fabrication is around 10 nm and the surfaces are rough, resulting in protrusions and inhomogeneities in the region of closest approach. Thus EBL is not suited to plasmonic interactions in the strong coupling regime, a regime of particularly high interest. In addition, nanofabricated particles contain not one but many crystalline domains. Single crystal structures have recently been shown to have superior optical properties compared to their lithographically fabricated counterparts [102,103]. For example, the single crystal nature and thus atomically smooth surfaces of metal nanowires significantly increases the propagation length of plasmon excitations (compared to that observed in lithographically fabricated structures) due to a reduction in the far-field scattering [104,105].

Investigations of the interparticle coupling at close interparticle approach were initially carried out via the fortuitous formation of colloidally synthesized nanoparticle dimers [96,106,107,89]. Resonances in dimers have been measured and modelled in detail for spheres and spherical disks. The key results, found for both EBL formed and colloidal nanocrystal dimers, are the shift to longer wavelengths of the longitudinal mode and a weaker blue-shifted transverse mode. The focusing of the electromagnetic field by metal particles allows the near-field of one particle to interact and hybridize with that of another. The near field interaction between nanoparticles is highly distance-dependent and has been described using an electromagnetic analogue of molecular orbital theory, the plasmon hybridization model [108], which highlights the asymmetry introduced by dimer formation [86,95,98,108]. The hybridization diagram for two spheres, along with expressions for the distance dependence are shown in Fig. 4 [86] along with the near-field map and induced surface charge distribution for spherical dimers, as calculated using the boundary element method (BEM) [99]. When the incoming electric field is oriented along the interparticle axis (for a given particle pair), the near fields couple in a manner analogous to a bonding interaction ($\sigma$-bond) and the electric field is focussed in the interparticle gap, resulting in a significant red-shift of the plasmon resonance [91,109,94,92,107,89,110,90]. When the polarization is oriented perpendicular to the interparticle axis on the other hand, their near fields couple in a non-bonding type of interaction ($\pi$-bond) and a very small blue-shift of the plasmon band is observed [91,90,94]. For each of these arrangements the other possible interaction mode is a dark mode which, in a completely symmetric monodimer, cannot be excited by light.

The optically inactive, dark modes have been investigated using more specialized microscopy techniques, although generally only for structures containing single crystals without randomly oriented crystal grains. The dark modes may be excited by an electron beam and its energy determined via electron energy loss spectroscopy (EELS) [111], although the relationship of the EELS energy profile to the optically determined plasmon resonance is unclear. As an alternative to this approach, symmetry breaking via confocal two-photon photoluminescence mapping allows the spatial mapping of both the longitudinal and transverse modes [103]. It has also been predicted that the dark mode may be excited via coupling to an optically active particle, leading to electromagnetic induced transparency [112]. Calculations within the electrostatic approximation have predicted that the dark modes have large evanescent fields combined with low radiation damping and therefore might provide a means to transmit energy through nanosystems while incurring minimal energy loss [113,114]. The interaction of a continuum (or broad) resonance with a narrow resonance at the same energy leads to a Fano (or Fano-like) resonance [115].

The distance dependence of the near-field interaction between nanoparticles has been exploited for measurement of distances in biological systems by Alivisatos and Liphardt [9,36]. For regions of intermediate interparticle separation, that is, distances between around 4 nm and 2.5 times the particle diameter (the coupling limit), the distance dependence of the plasmon resonance coupling is well understood. The larger the observed spectral shift, the stronger the coupling and the greater the localization of the near-field between the two particles (for a bonding interaction) [116]. The plasmon resonance position may be calculated relatively easily in this regime using classical theories including the plasmon hybridization model [98], the discrete dipole approximation (DDA) [94], finite-difference time domain (FDTD), and surface integral approaches [113,117,118] including BEM [99]. At smaller separations it has been shown that coupling to higher order modes (for example the quadrupole resonance) becomes increasingly important. Methods which do not take these into account become inaccurate and the inclusion of several orders of multipoles is necessary [114,101,49]. For excitation of the longitudinal modes, the red-shift has been approximated as either a $d^{-3}$ dependence [91], or as an exponential function. It is found that normalization of the plasmon resonance shift to the particle diameter (or for rods to the rod length) leads to a size and material-independent measure of the coupling [90]. Both the approximations ($d^{-3}$ and exponential distance dependence) break down for small interparticle separation [96,100].

At very small interparticle separations, less than 1 nm, the accuracy of the classical descriptions becomes questionable and a quantum mechanical description has recently been developed [100]. The calculations predict that at these separations, the finite electron density in the interparticle gap becomes significant and these screen the electromagnetic field in this region leading to smaller plasmon shifts than predicted using the classical models. The tunnelling of electrons from one particle to the other, creating a continuum between the touching and non-touching particles, also becomes a possibility at these separations. For the sphere dimer system, there are two distinct ''strong coupling'' regimes; the classical regime for separations >1 nm, and for separations smaller than 0.5 nm a ''quantum regime'', where it is predicted that a charge-transfer band appears due to the electrical tunnelling between particles [100]. These regimes are very difficult to access experimentally. Lithographic fabrication cannot reach this resolution. A few experimental investigations of dimers composed of single crystals of spheres [107,106,49] and rods [96] have appeared. These mainly relied upon the serendipitous formation of the dimers in single particle studies with the

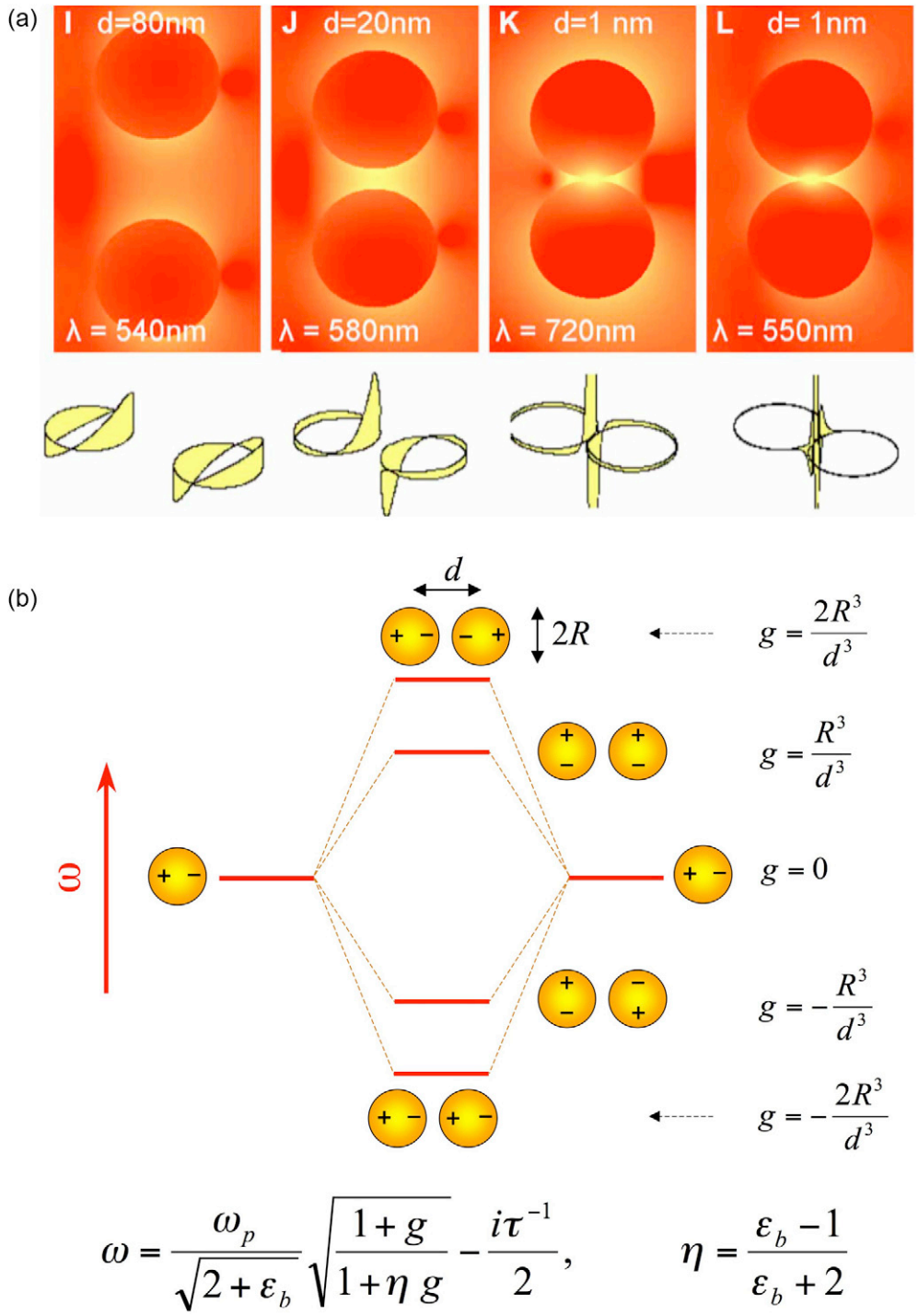


**Figure 4** (a) Near-field maps and the corresponding induced surface charge distributions for two neighbouring gold spheres (radius = 60 nm) as a function of their separation *d* and wavelength λ. Reproduced from Romero et al. [99]. (b) Plasmon hybridization diagram for the interaction of two spheres. The modes of the interacting system are derived from the eigenfrequencies of the two-particle DDA equations. The mode frequencies correspond to the formula quoted at the bottom, with values of *g* shown in the insets and containing the dependence on centre-to-centre separation, d. Retardation effects and higher-order multipoles have been neglected in these expressions. Reproduced from Myroshnychenko et al. [86].

dimers identified via the correlation of the spectra with an electron micrograph of the particles. In these cases, the distance was determined by the thickness of the ligand shell. The experimental demonstration of these quantum mechanical regimes thus remains a challenge. A second important challenge is controlling and minimizing the variations in interparticle separation for single nanocrystal dimers.

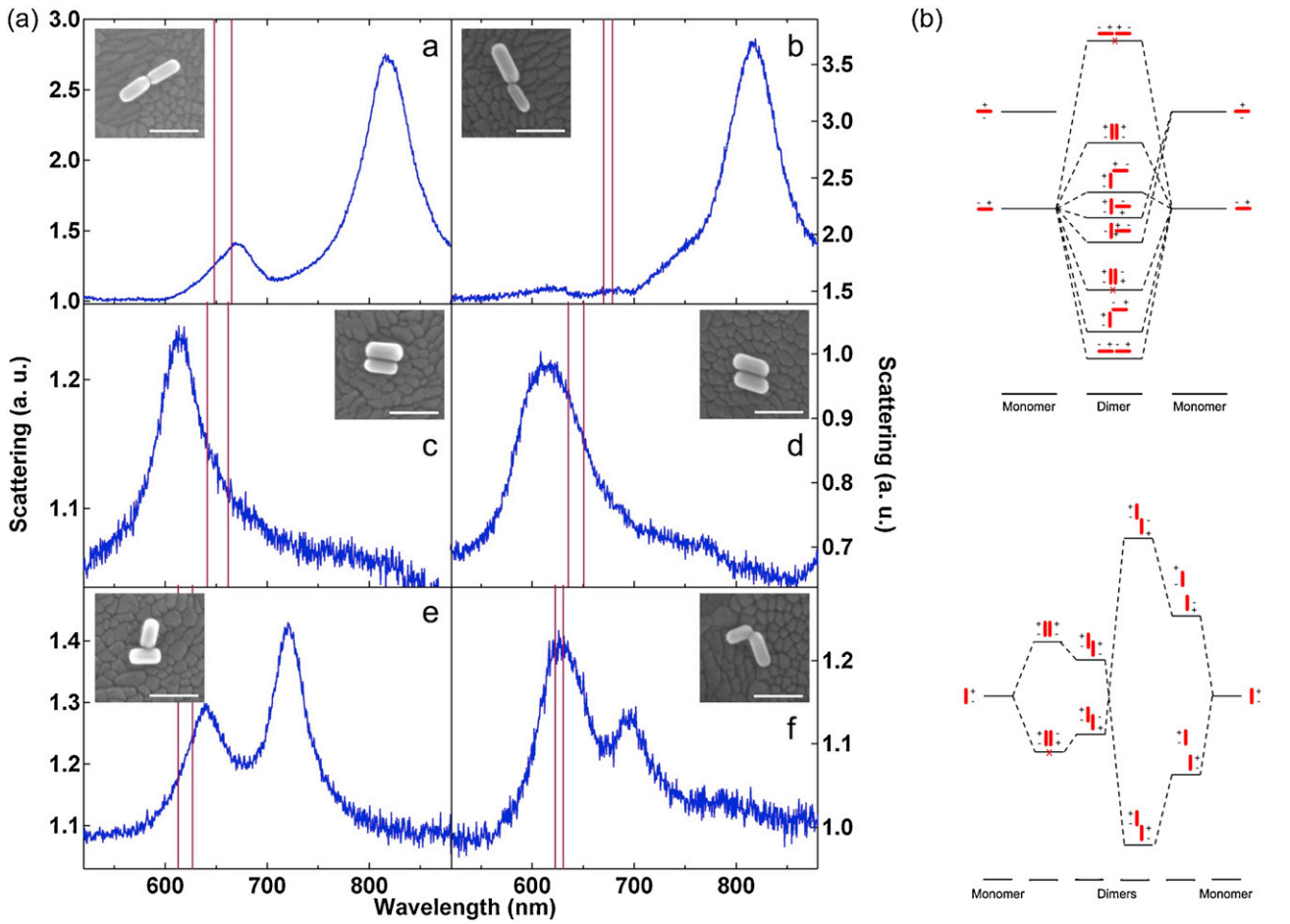


**Figure 5** (a) Scattering spectrum for two rods aligned (a and b) end to end, (c and d) side to side, (e) in a T configuration and (f) in an L configuration, all on ITO and in air. Insets show SEM images of the structures. Scale bars = 100 nm. (b) Plasmon hybridization schemes for (a) rod dimers in different geometric arrangements and (b) rods initially arranged side-to-side and then increasingly longitudinally offset as a function of the center-to-center offset. Reproduced from the work of Funston et al. [96].

Introducing further asymmetry into the coupled system by moving from zero dimensional spheres to one dimensional rods dramatically increases the number of coupled modes possible within the system [96]. A qualitative plasmon hybridization diagram for the coupling of two rods in different, but simple, highly symmetric geometries is shown in Fig. 5(b), while the experimentally determined scattering spectra for these geometries are shown in Fig. 5(a). It is evident that coupling between both the longitudinal and transverse plasmon resonances of the rods is possible; however the coupling is strongest for longitudinal—longitudinal modes as might be intuitively expected. The practical upshot of this is that, while both 'L' and 'T' nanorod geometries form models for T junctions in optical circuits, coupling within the T geometry is not particularly strong as it is a longitudinal—transverse interaction and excitation of the longitudinal mode of either rod does not lead to significant delocalization of this energy into the other rod. The L geometry, on the other hand, involves strong coupling between two longitudinal modes with efficient delocalization of the plasmon resonance throughout the full structure [96]. For nanorods aligned both end-to-end and side-to-side, one of the fundamental modes are dark, but a slight lowering of the symmetry of the system causes these dark modes to acquire a dipole moment and become optically bright [96]. The asymmetry of the rods also leads to a number of different trajectories for the approach of two rods into a common alignment [96]. Further extension of these geometries to nanorod trimer structures confirms the above points [119]. These results highlight the importance of orientation on the coupling of anisotropic nanoparticles such as rods. Small changes in the rod orientation lead to relatively large changes in the plasmon interaction, particularly at close approach. Thus, in these systems, the coupling and therefore the position of the plasmon resonance may be controlled through nanoparticle separation, angle and interaction geometry [96,120—122].

The results in Fig. 5 highlight the importance of the interaction geometry for assemblies containing more than two nanospheres. Both one-dimensional and two-dimensional structures are possible, and the DNA hybridization schemes must be carefully chosen to preferentially yield the desired geometry. One-dimensional structures containing a rela-

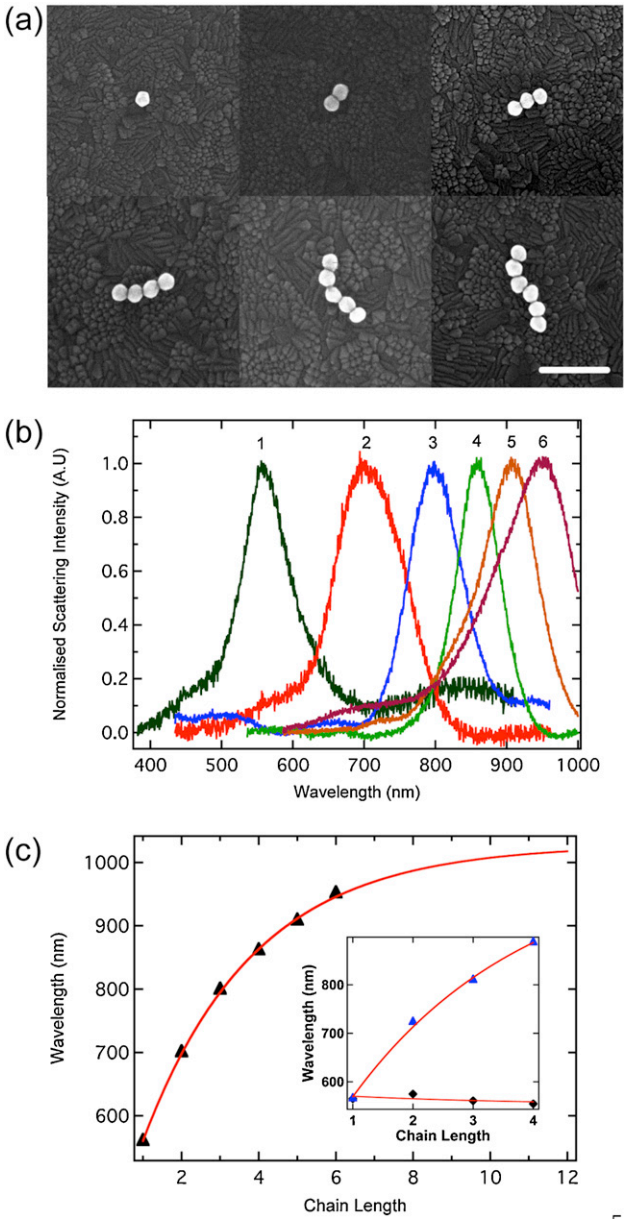


**Figure 6** (a) SEM images of self-assembled nanoparticle chains. Mean diameter of gold particles is 64 nm. Scale bar = 250 nm. (b) Normalized spectra of the nanoparticle chains shown in (a). (c) Maximum wavelength of longitudinal plasmon band plotted against number of particles in the given nanoparticle chain. Data points were obtained using a Lorentzian fit to the spectral data in Fig. 2. Inset shows a plot of both the longitudinal (blue solid triangle) and transverse (black solid diamond) bands with increasing nanochain length. Exponential fits are shown for each set of data (red lines) with the exponent fixed to have magnitude equivalent to that determined for the longitudinal mode, but with opposite sign, for the transverse bands to maintain an exponential fit. Reproduced from Barrow et al. [49].

tively uniform, linear array of crystalline nanoparticles are of particular interest for optoelectronic applications while two-dimensional structures have been found to exhibit unique optical properties including Fano-like resonances and highly enhanced electromagnetic field hot spots.

## One dimensional structures

The most basic self-assembled structures are one dimensional chains. These are assembled via the functionalization of metal nanoparticles with two complementary oligonucleotide strands (Fig. 1(a)) [49]. Following initiation of the assembly with PBS buffer, different assembly times are used to favour either lower order (dimer and trimer) or higher order (tetramer, pentamer and hexamer) linear structures. An assembly time of 1 min favours the formation of dimers and lower order structures, whereas 5 min favours longer chain structures forming. Many aggregates and nonlinear structures are also evident in such assembled samples, necessitating the use of correlation between the optical properties and the assembly geometry [123]. SEM images of one-dimensional nanoparticle chains containing 1—6 gold nanoparticles with 64 nm diameter are shown in Fig. 6(a). The oligonucleotides used for the assembly should give interparticle spacings of 5—6 nm, however due to the relatively large size of the nanoparticles they were found to be in PLC and separated only by the ligand shell, approximately 1 nm. The observed interparticle spacing is consistent with the interparticle spacing observed for other CTAB covered Au nanoparticles where the nanoparticles were not specifically linked together prior to their deposition on the substrate, but formed randomly via a combination of van der Waals and capillary forces [96,119]. The use of larger particles in the linear chains complicates the modelling of these structures as retardation becomes an important factor in the modelling. This adds to computational time and complexity.

The wavelength of the most intense scattering peak is shown as a function of the number of particles in a particular chain in Fig. 6(b) [49]. This resonance is identified as a longitudinal coupling mode along the length of the nanoparticle chain, and this is borne out by its response to polarized excitation light and is consistent with electrostatic eigenmode method (EEM) and boundary element method (BEM) modelling [49]. As the nanoparticle chain length increases from 1 to 6 particles, the wavelength of the most intense scattering peak red shifts, asymptoting to a value of $\lambda_\infty = 1028$ nm for a chain of about 10—12 particles (see Fig. 6(c)). The observed exponential trend is in accordance with the theoretical models of Maier et al. [15] and Fung et al. [124] and a plateau at a chain length of approximately 10 has been theoretically predicted for nanoparticle chains at small interparticle separations (<5 nm) using rigorous EM theory [125—127,114]. A second, less intense resonance is observed at wavelengths ranging from 500 to 550 nm, which is attributed to the collective mode transverse to the axis of the nanoparticle chain. [49]

Despite the complexity of modelling the obtained nanoparticle chains, using the EEM formulation [117,113] it was found that the most intense resonance peaks are due to

a single resonant mode, assigned as the longitudinal coupling mode with an energy dependent upon the interparticle coupling strength (in turn a function of the nanoparticle size and interparticle separation) and the dielectric constant of the medium. Neither BEM [128,129] or EEM [117,113] modelling is able to quantitatively predict the energy of the longitudinal plasmon mode, although for EEM the agreement is better when coupling from a larger number of higher order multipolar modes is included. Retardation, quantum effects and the effect of the substrate were not taken into account in the calculations.

## Two dimensional structures

The design and use of appropriate DNA coupling schemes lead to the formation of higher-order, two-dimensional assemblies. These include most commonly trimer structures with various symmetries, including the highly symmetric $D_{3h}$ structure [130—132] with a few reports of tetramers, although none with perfect cubic symmetry [130,133,47].

The DNA hybridization schemes for the formation of trimers and tetramers become increasingly more complex. The greater complexity generally results in lower yields of the desired structure, and the greater number of nanoparticles leads to higher chances of asymmetry within the structures [135,46]. For example, for assembly via the DNA hybridization schemes shown in Fig. 1(a), the yield of dimers was 26%, whilst the corresponding yields for the assembly of trimers and tetramers were 5.6% and 3%, respectively. Despite these obstacles, the development of effective strategies to assemble discrete two-dimensional structures containing three to five nanoparticles with a defined geometry is an important step in the formation of more complex clusters with novel optical properties. Additionally, the discrete structures themselves can display useful optical properties, including strong enhancement of incident electromagnetic fields [130,136]. Asymmetric assemblies of this type also display Fano-like resonances due to interference of the optical field of the narrow, dark (or subradiant) mode with the field of a continuum, in this case the broad band of the bright plasmon resonance (Fig. 7).

The SEM images of a single particle, a 2 particle chain (dimer), a 3 particle triangle (trimer), and three variations of a 4 particle tetramer, the square aligned tetramer (bottom left), the slightly rhombic tetramer (bottom middle) and the extremely rhombic tetramer (bottom right) are shown in Fig. 8. Each structure shown is comprised of gold nanoparticles that are on average 64 nm in diameter and thus, as before, the nanoparticles are observed to be in PLC with an interparticle spacing of approximately 1 nm (the DNA strands used for the assembly contained 16 bp). These were assembled using the dimer, trimer and tetramer DNA hybridization schemes of Fig. 1(a).

Highly symmetric trimer structures belong to the $D_{3h}$ point group. The symmetry of such a trimer is expected to lead to a structure displaying one bright, in-plane, doubly degenerate plasmon mode [137]. This mode has been labelled according to its irreducible point-group representation as a sum of the $E'$ modes, with the degeneracy a result of the high symmetry [137]. The $E'$ modes can be classified into two pairs of doubly degenerate modes, one pair representing the high-energy antibonding modes and the other pair corresponding to bonding modes in the low-energy region of the visible spectrum [137,131]. It is pertinent to note that the lowest energy dipole in-plane mode for a circularly arranged $D_{3h}$ trimer, the $A_2'$ mode is predicted to be dipole inactive, unable to couple to an incoming electromagnetic light field and therefore a dark mode. It does, however, support a ring-like displacement current and, as such, may be labelled a magnetic mode [138,137]. This is also the case for higher-order circularly arranged structures, for example the tetramers referred to below (with their appropriate symmetry designations). Given the degenerate nature of the lowest energy in-plane bright mode, a completely symmetrical $D_{3h}$ structure is expected to show very little dependence upon the angle of in-plane polarization of the excitation source (disregarding the effect of the substrate which will introduce an additional, albeit slight asymmetry [139,140,133]). The lowest energy out-of-plane bright mode is blue-shifted with respect to the plasmon resonance of the uncoupled particles. The polarization-dependent plasmon resonance of a trimer structure assembled using the trimer DNA assembly scheme in Fig. 1(a) is shown in Fig. 9(a). The plasmon resonance of the trimer structure shown here exhibits one predominant plasmon mode with $\lambda_{max}$ = 748 nm with very little polarization dependence, an indication of its high symmetry. As shown in Fig. 9(b), the theoretical scattering spectrum of an identical trimer cluster calculated via the finite-element method (FEM), COMSOL Multiphysics 3.5a, also exhibits one predominant, low-energy plasmon resonance at $\lambda_{max}$ = 695 nm and another, less intense resonance at 580 nm. The low-energy mode corresponds to the optically active $E'$ bonding mode and shows very little dependence on the polarization angle, consistent with the experimental results.

In this highly symmetric trimer, the magnetic mode of $A_2'$ symmetry cannot directly interact with the dipolar bonding mode $E'$. However, breaking the symmetry of the trimer system does lead to a strong interaction between these modes [131,132]. The scattering spectrum of the second trimer, shown in Fig. 9(c and d), is a more typical result from DNA self-assembly. Inspection of the SEM micrographs of the two trimers in Fig. 9 however reveals very little apparent difference (at the resolution of the images) between the two trimer structures. The spectral features observed are indicative of a lowering of the symmetry of the trimer from the ideal $D_{3h}$ symmetry [131,132,141,130]. These include an increase in the number of resonances observed in the scattering spectrum as well as a significant dependence upon the polarization of the incoming electric field. One possible way the symmetry may be broken is by an increase of the interparticle separation between only two of the nanoparticles, with the other interparticle separations remaining identical and smaller (relative to the elongated interparticle distance), which reduces the symmetry to $C_{2v}$. In this case, the magnetic mode $A_2'$ transforms into a mode of $B_2$ symmetry. When the polarization is perpendicular to the gap elongation (0°, as shown in Fig. 9(d)), the bonding electric mode $E'$ transforms to a new mode with $A_1$ symmetry, thus these two modes do not interact. However, when the polarization of the electric field is 90° (Fig. 9(d and e)), and therefore parallel to the direction of gap elongation, the magnetic mode is able to effectively interact with the

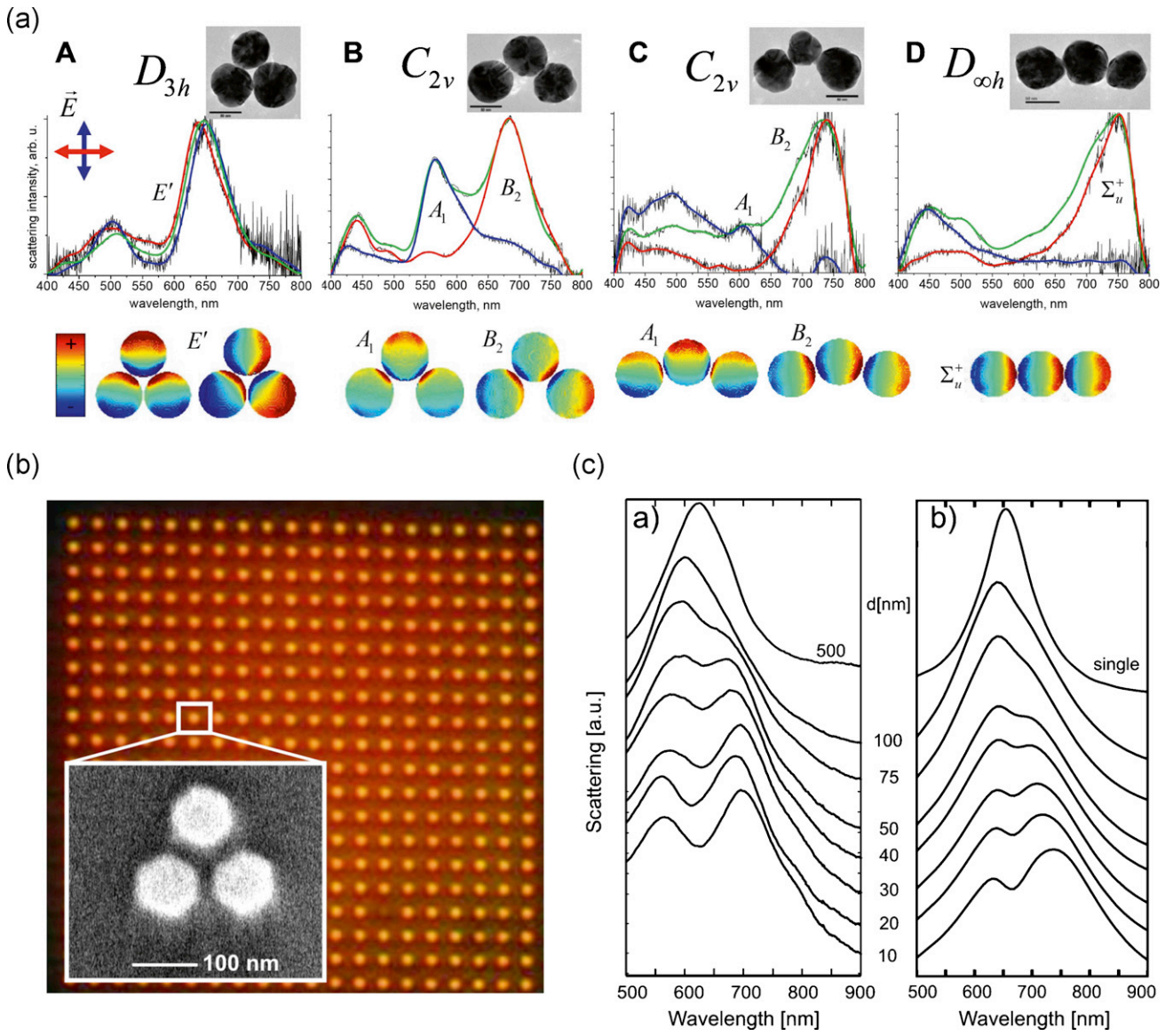


**Figure 7** (a) Scattering spectra of silver nanoparticle trimers showing mode splitting due to gradual opening of the vertex angle. Thin black lines — raw experimental data; colour lines — low pass filter applied. The clusters are excited by either nonpolarized light (green) or by light linearly polarized along either the longitudinal (red) or transverse (blue) directions (which are indicated by arrows of matching colours). The polarized spectra are normalized to the corresponding peaks of the nonpolarized spectra. Plasmon mode symmetries of the bonding modes are marked. TEM images of the clusters are shown in the insets (the bars are 50 nm). Calculated surface charge distributions of the selectively excited bonding modes are shown below the spectra. Reproduced from Chuntanov et al. [131]. (b) Dark-field microscopy image of an array of silver trimers on glass in immersion oil. Each red dot corresponds to one individual trimer composed of silver disks with diameter (*D*) 100 nm and height (*h*) 25 nm. Inset shows a SEM image of one representative Ag trimer. Reproduced from Alegret et al. [134]. (c) Experimental and simulated spectra of silver trimers from the work of Alegret et al. [134].

electric mode, as they transform into modes of the same symmetry, $B_2$, and Fano-like resonances are observed. The surface charge densities associated with the three observed modes, including the Fano-like mode, for this excitation geometry are shown in Fig. 9(e). The calculated scattering spectrum of the asymmetric trimer modelled in this manner closely matches the experimentally measured spectrum of the trimer shown in Fig. 9(c).

These results are consistent with the literature describing the optical properties of chemically synthesized and assembled gold nanoparticles. The focus of previously reported bodies of work, most notably by Chuntonov et al. [132,131], has been the effect of the symmetry breaking on the coupling within the nanoparticle structure and the consequences of this on the optical properties of the assembly. Only a few, highly symmetric chemically assembled trimer structures with one predominant, and polarization independent, low energy plasmon resonance, such as that shown in Fig. 9(a) have been reported [130,131]. Even slight polydispersity in the size of the nanoparticles within the

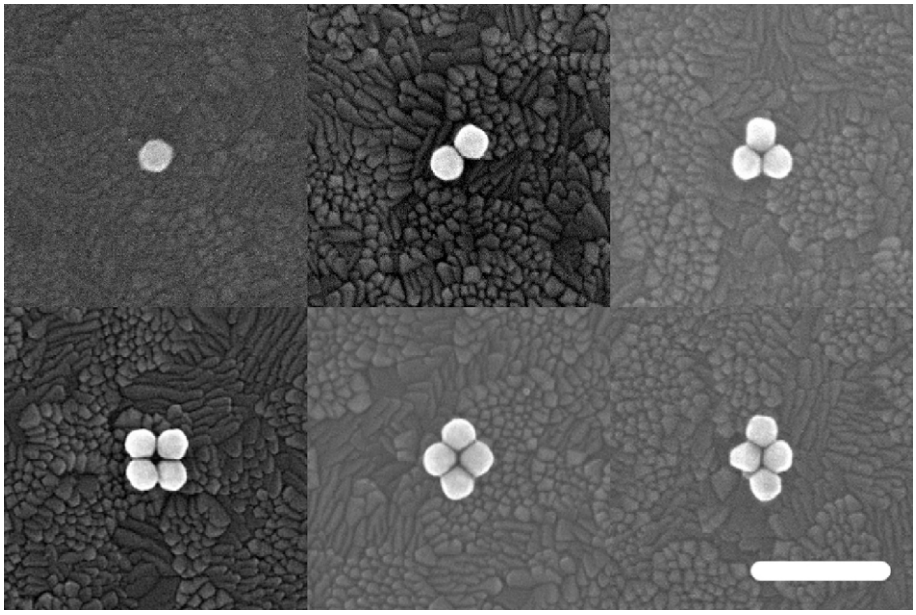

**Figure 8** SEM images of a single gold nanosphere (top left), a dimer (top middle), a trimer (top right), a square aligned tetramer (bottom left), a slightly rhombic tetramer (bottom middle) and an extremely rhombic tetramer (bottom right). Gold nanospheres have an average diameters of 64 nm. Scale bar = 250 nm.

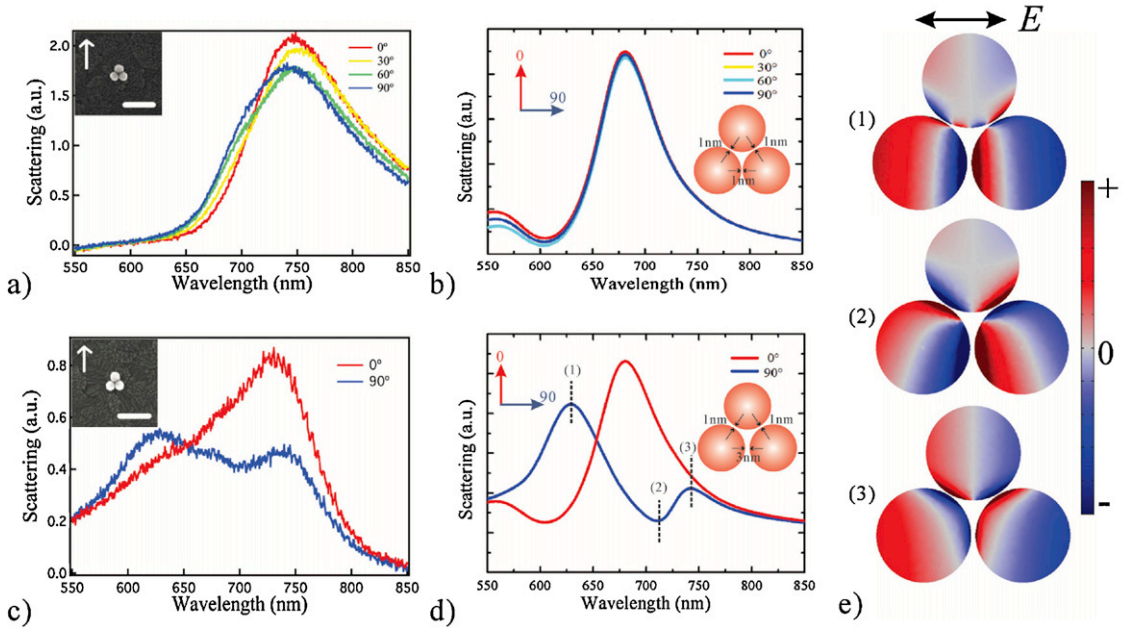


**Figure 9** (a) Experimental scattering spectra of the assembled nanoparticle trimer shown in the SEM micrograph inset, as a function of the polarization of the exciting electric field (0° is parallel to the arrow shown on the SEM inset). The gold particles are on average 64 nm in diameter, and the spectra were collected on an ITO coated glass substrate in air. Scale bar = 250 nm. (b) Polarization dependent calculated scattering spectra, for a completely symmetrical nanoparticle trimer, with interparticle separation of 1.0 nm. (c) Scattering spectra of the assembled nanoparticle trimer shown in the SEM micrograph inset with the electric filed polarized at 0° and 90° to the arrow. (d) Calculated scattering spectra for a trimer with unequal interparticle separations (1 nm, 1 nm and 3 nm) with the incoming electric field polarized at 0° and 90° as indicated in the inset. A Fano resonance is apparent when polarization angle is 90°. (e) Surface charge density plot at different modes for polarization angle is 90°. The relevant wavelengths are indicated in (d). (1) Charge oscillations on nanoparticles oriented in the same direction, yielding a coupled electric bright mode. (2) The circulating charge oscillations show the dark mode which could suppress the radiative losses. (3) Surface charge distribution shows a largely coupled electric dipole moment. In the FEM calculation, the particles cluster of interest were delimited by perfectly matched layer (PML), to prevent unwanted reflections by efficiently absorbing the scattering off the particles. All calculations were performed in an effective embedding medium (herein, $\epsilon_{eff} = 1.6384$ for trimer). The optical constant of gold was taken from Johnson and Christy [142]. S-polarized incident light at 61° to the normal of the cluster plane was chosen in accord with the experiment.

assembly leads to asymmetric trimer structures [132]. In addition, at the close approaches investigated here even a small difference in the interparticle separation, perhaps due to the facetting of the particles, leads to symmetry breaking and relatively large changes in the scattering spectrum of the assembly. This is highlighted by the trimer structures and their spectra shown above in Fig. 9, in which the trimers both appear to be highly symmetric at the resolution of the micrograph, however their spectra are very different with one spectrum displaying characteristics of a lower symmetry than the ideal $D_{3h}$. Hence, it may be concluded that the relatively unpredictable nature of the interparticle separation achieved via DNA assembly is problematic and make it difficult to achieve completely ideal symmetry. The use of smaller nanoparticles may help to obviate this issue. It is notable that ideal $D_{3h}$ symmetry and predictable interparticle separation for large numbers of structures are difficult without using lithographic fabrication methods. While lithographic methods are unable to produce the small interparticle separations achievable via self-assembly techniques shown here, the regularity of the structures result in a good agreement between the calculated and observed spectra for trimers of silver nanodisks [134].

The difficulty in achieving perfect symmetry in assembled structures containing larger numbers of assembled nanoparticles, such as tetramers, becomes even greater. Fig. 8 shows SEM images of three tetramers with slightly different symmetry alignments of the four nanospheres. The nanostructure on the bottom left of Fig. 8 contains nanospheres aligned at the vertices of a square giving $D_{4h}$ symmetry, whereas the other two structures in the bottom middle and bottom right SEM images present varying degrees of rhombic alignment. All of the particles in each structure have small inter-particle spacings (approximately 1 nm). These structures were achieved using the one, identical synthetic assembly scheme shown in Fig. 1(a). The few self-assembled tetramer structures that have been previously reported all display rhombic nanoparticle arrangements of varying degrees [130,133,47]. Using the assembly method outlined in this work, only 6% of tetramers exhibited near-perfect symmetry, with rhombic tetramers accounting for 73% and the remaining 21% having alignments between these two extremes.

Much like a trimer with equal particle size and interparticle spacing, a completely symmetric $D_{4h}$ assembly should show one predominant low energy resonance which has little dependence upon polarization. In this case, the low-energy mode corresponds to the optically active doubly degenerate in-plane bright mode, a sum of the modes with symmetries from the $E_u$ irreducible representation of a tetramer with perfect $D_{4h}$ symmetry [137]. The double-degeneracy leads to little polarization dependence and the scattering spectra calculated using FEM (as above) are shown in the lower left inset of Fig. 10(c). However, for self-assembled structures at this very small interparticle separation, the spectra of the assembled tetramers (even those apparently of the $D_{4h}$ symmetry), usually display multiple low-energy modes, the relative intensities of which have a significant dependence on the polarization of the incoming field, as can be seen for the tetramer shown in Fig. 10(a). This indicates that the structures contain small, but significant asymmetries, such as differences in nanoparticle shape, facetting and size as well as variation in placement (from a perfect square). Because of this, the modelling and analysis of these structures will necessarily be intimately structure specific.

The lowering of the symmetry from $D_{4h}$ results in a more rhombic structure. The scattering spectrum of an assembly with a rhombohedral geometry is shown in Fig. 10(c),while the inset presents an SEM micrograph of the assembled structure. The spectrum displays a number of resonances, indicative of symmetry breaking from ideal $D_{4h}$ geometry, and is highly polarization dependent. FEM calculations of the rhombic structure shown in the inset in Fig. 10(d) predict that at a polarization angle of 0°, the spectrum should display one predominant resonance, whilst at 90° polarization, a minor Fano-like minimum should emerge at 750 nm. The relative peak intensities and energies of the experimentally determined spectra, as well as the overall trend for the polarization dependence agree reasonably well with this. The tetramer shown in Fig. 10(b) has a more extreme rhombic alignment than the tetramer shown in Fig. 10(c). The more rhombic tetramer also agrees with the model shown in Fig. 10(d) as a Fano resonance can also be seen in the spectrum at 30°. A greater degree of symmetry breaking will result in this Fano-like minimum becoming more pronounced. Similarly, it has been reported that rhombic assemblies of large metal nanoshells with silica cores (180 nm outer diameter) display a pronounced and robust Fano-like resonance due to the interaction of the lowest energy dark mode with the broad bright mode [133]. The theoretical and calculated scattering spectrum of 60 nm diameter gold nanospheres aligned in a tetramer with rhombic geometry has been reported [130]. Whilst not commented on or specifically assigned in the text, some structure on the low energy side of the major plasmon resonance was observed. This was more obvious for the calculated spectrum (simulated using multiparticle generalized Mie theory (GMT)) [130]. Structures such as this displaying a Fano-like resonance have been proposed for use within SERS sensing [130], yielding a much greater figure of merit (FOM) than individual silver or gold nanoparticles.

## Three dimensional structures

The formation of highly symmetric and well-defined circular structures and the extension of these to three-dimensional structures is a necessary prerequisite for plasmonic applications such as metamaterials and cloaking [19,18,143]. Concentrated solutions of three-dimensional, symmetric tetrahedral structures have been identified as potential metafluids, that is liquid metamaterials based on specific, well-defined and three-dimensional clusters of metallic nanoparticles [143]. However, the fabrication of discrete three-dimensional structures of a specific geometry via self-assembly remains a challenge. Complex DNA hybridization schemes designed to achieve the formation of symmetric three-dimensional structures in solution have been reported; however the three-dimensional nature of these discrete assemblies either in solution or following deposition on a substrate has not been unambiguously proved

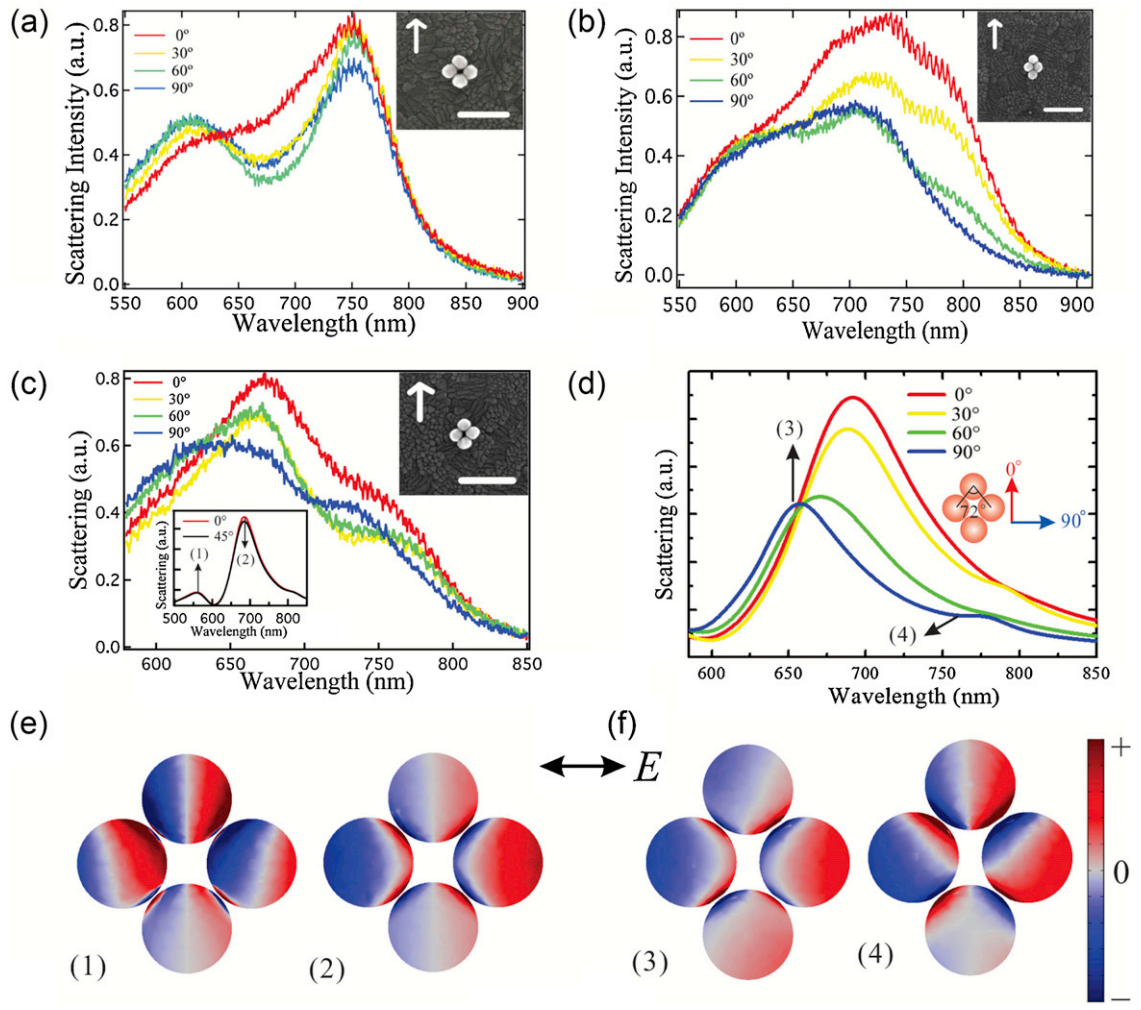


**Figure 10** (a and b) Experimental polarization data for a symmetric and rhombic tetramer, respectively. The insets in each image show SEM images of each structure with scale bars of 250 nm. (c and d) Experimental and calculated scattering spectra for a tetramer with a slightly rhombic distortion as a function of polarization. The upper right inset in (c) shows an SEM image of the tetramer, scale bar = 250 nm. The lower left inset shows the calculated polarized spectra for a symmetric tetramer, the surface charge distributions for which are shown in (e), in which picture (1) magnifies the coupled multipolar modes, and picture (2) exhibits the strongly coupled dipole modes. The surface charge distributions for the asymmetric tetramer modelled in (d) are shown in (f), which clearly exhibit the coupled electric mode and Fano-like resonance mode. Gap distances are all 1 nm in simulation.

to date [46,47]. In both these reports, the deposition and subsequent drying of the assemblies on a substrate for electron microscopy led to the collapse of the solution-based three-dimensional structures. As a direct result of this, the spectral characterization of individual three-dimensional structures with known geometry and interparticle separation has not been reported. Structures of this type, for example a tetrahedron with the nanoparticles at the vertices, may be expected to have an optical spectrum that is completely independent of either the polarization or the angle of the incident light beam. This, combined with pronounced hot spots formed within the structure via the interaction of the individual nanoparticles make these structures particularly powerful for SERS applications [144].

One approach to the fabrication of highly symmetric, three-dimensional structures is to exploit the assembly procedure described for two-dimensional structures. A schematic of the approach is outlined in Fig. 11. The formation and deposition of two-dimensional structures is carried out according to the methods outlined in Fig. 1(a), and the Supporting Information, with a hybridization time of approximately 5 min. Assembly results in two-dimensional trimer bases as expected but tetramers and pentamers also form as byproducts [144]. To build three-dimensional structures, a second DNA functionalization step (with a different DNA sequence) is undertaken. This is carried out after the structures have been coated onto the substrate using another nanoparticle pre-functionalized with the complementary oligonucleotide.

The yields of the 3D structures formed by this method were found to be 1.0%, 1.1% and 0.15% for the 3D tetramer, pentamer and hexamer, respectively. Taking into account the fact that the initial yield of 2D trimers is 5.6%, the yield of 3D tetramers from 2D trimers is 18% [144].

SEM images of a three-dimensional tetrahedron, square pyramid and hexamer fabricated using this assembly

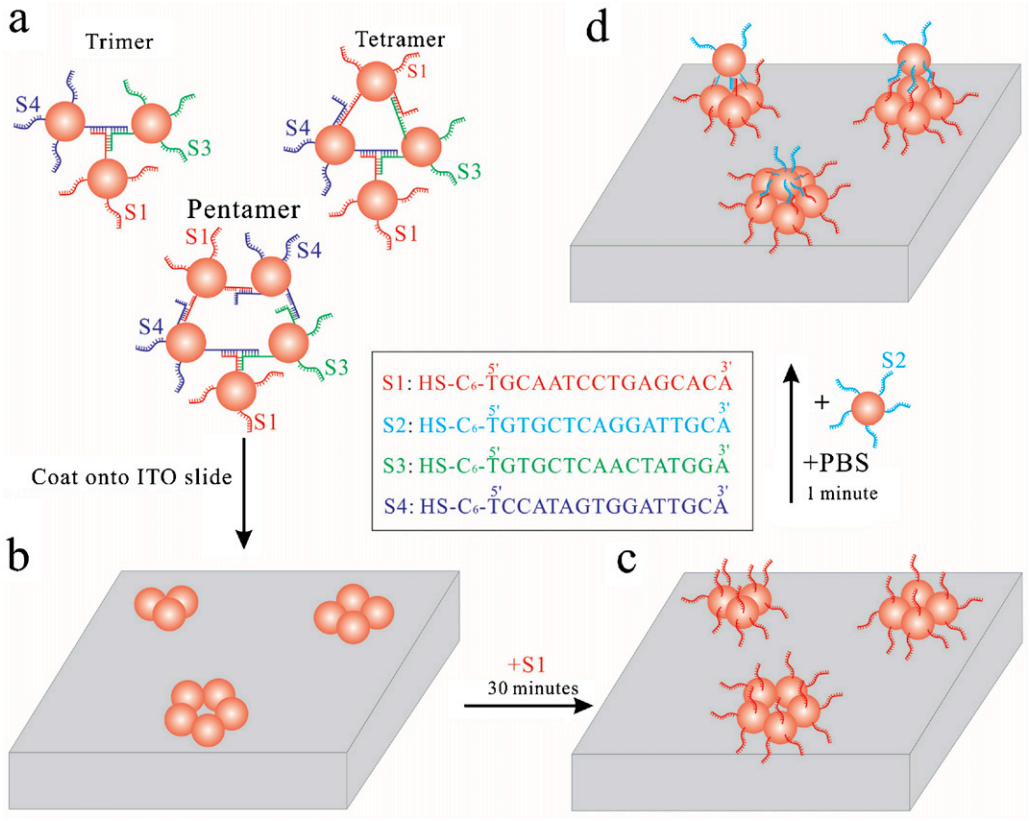


**Figure 11** The DNA meditated assembly scheme for producing 3D nanostructures is shown. (a) The hybridization mechanism in shown for producing the base of the 3D nanostructures. (b) Once assembled in solution, the based of the 3D nanostructures is coated onto and ITO-glass coverslip. (c) Structures that have been coated onto coverslips are then coated with a layer of thiolated DNA. (d) A second assembly step is then used to deposit a particle on top of the pre-coated structure. The base sequences of the DNA strands are shown in the inset.

approach viewed from above and at a 52° angle are shown in Fig. 12(a). It is clear from the SEM images that these structures are three-dimensional. The tetrahedral structure is highly symmetrical, and, as the two-dimensional trimer base is close-packed, the positioning of an apical nanoparticle within the hole leads to a fully close-packed structure. In contrast, for the pentamer, the two-dimensional structure is cubic. Consequently, the central hole is larger and the resulting three-dimensional structure is not close-packed. The same is observed for the hexamer structure.

The polarization averaged scattering spectra of all these three-dimensional structures display two major resonances in the visible region (Fig. 12(b)), a low energy peak around 670—700 nm and a higher energy resonance at 540—570 nm, see for example the spectra of the three-dimensional hexamer in Fig. 13. For the very small interparticle gaps created within these structures, quadrupole and octupole modes can also be excited and the higher energy peaks observed in all the three-dimensional structures consist of a number of these higher-order modes. The low energy mode is due to the coupling of dipolar modes of the individual particles. For the structure with tetrahedral symmetry this mode is consistent with the $T_2$ irreducible representation of the $T_d$ point group [143]. Of the irreducible representations of the $T_d$ point group, only the triply degenerate $T_2$ has a non-zero net electrical dipole moment, and only the $T_1$ has non-zero net magnetic dipole moment, the latter supporting a ring-like displacement current across one of the faces of the tetrahedron [143]. The bases of both the three-dimensional square pyramid and the hexamer also support a ring-like displacement current leading to a non-zero net magnetic moment for these modes and imparting magnetic properties to the assemblies. In contrast to the centre nanoparticle in the fully planar heptamers, the presence of the upper nanosphere in the three-dimensional hexamer does not lead to a coupling of the magnetic mode of the lower ring with the electric modes. As a consequence a Fano-like resonance is not present in the three-dimensional structure (see Fig. 13(a and c)) whereas it is present in the fully planar structure [138].

An important difference between the three structures is that only the tetrahedron is three-dimensionally isotropic. The square pyramid and hexamer are isotropic for in-plane excitation and are expected to show little in-plane polarization dependence as discussed for the $D_{4h}$ structures described above. However, in contrast to the tetrahedron, for these two structures the energy of the out-of-plane resonances is different from that of the in-plane resonances. The small in-plane polarization dependence observed for all these structures confirms their high symmetry [144], although some polarization dependence is obvious. The scattering spectra for the three-dimensional hexamer structures show less dependence on the in-plane polarization than

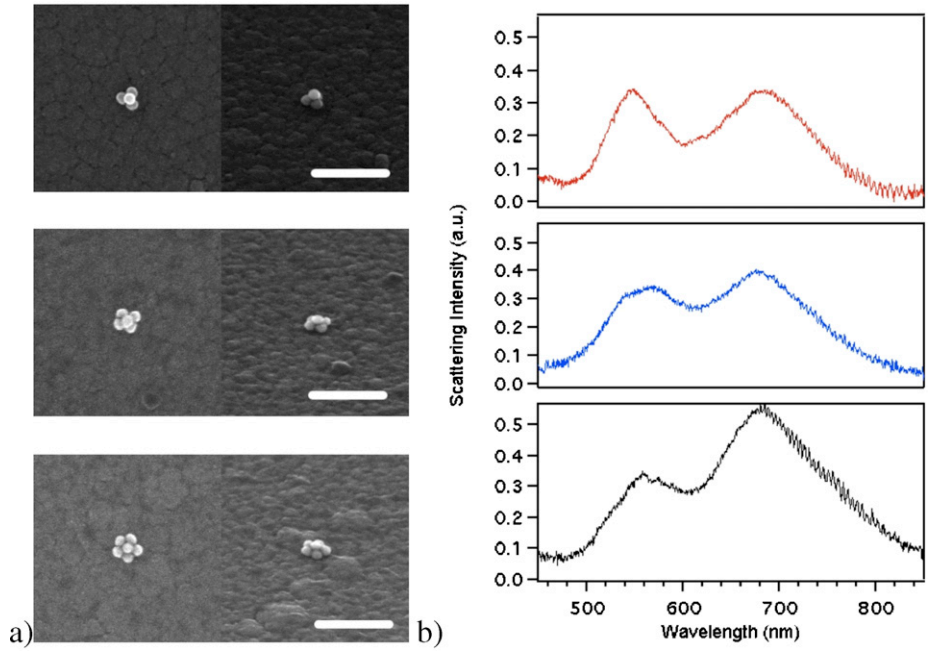


**Figure 12** (a) The SEM images of a gold nanosphere 3D tetramer (above), a 3D pentamer (middle) and a 3D hexamer (below), each viewed from above (left column) and from a 52° angle (right column). Gold nanospheres with diameters of 30 nm were used in assembling these structures. Scale bar = 200 nm. The spectra of the structures in (a) can be seen in (b), with the tetramer spectrum at the top, pentamer in the middle and hexamer at the bottom. The spectra were collected with non-polarized light.

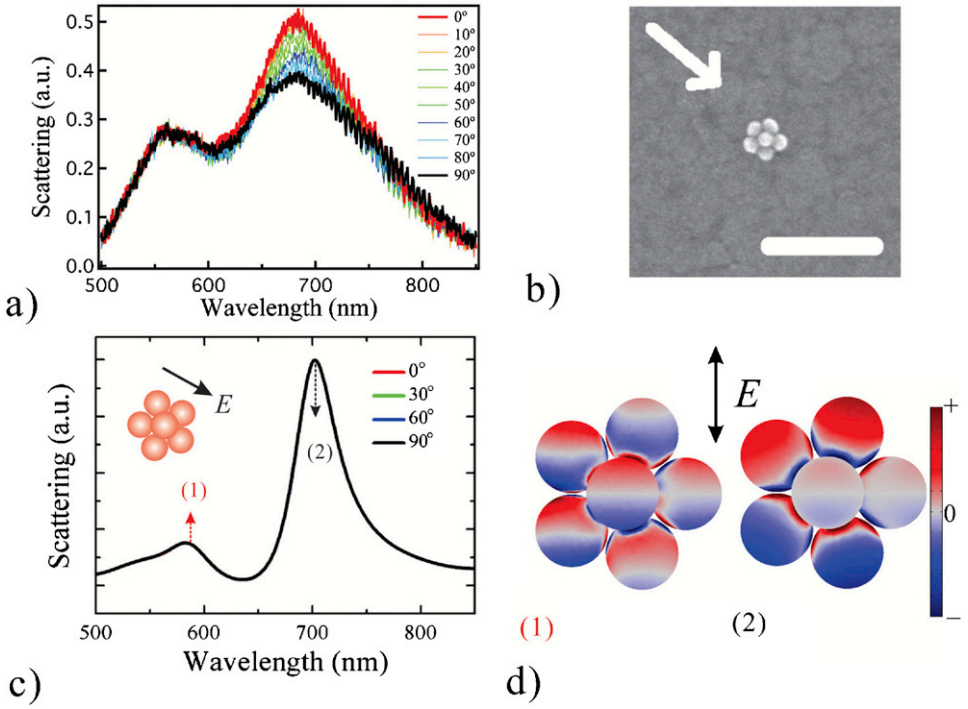


**Figure 13** (a) Optical response of a 3D hexamer. (b) The inset shows an SEM image of the hexamer, scale bar: 200 nm, arrow direction indicates polarization direction for 0°. (c) Corresponding calculated results for the spectra shown in (a). All polarized spectra overlap, highlighting the optical stability of the structure. (d) Surface charge distributions at 585 nm (marked as (1)) and 705 nm (marked as (2)), respectively. The surface charge distribution originated from multipolar modes is shown in (1); coupled dipole charges oscillations oriented in the same direction and exhibit an enhanced electric mode in (2).

observed for the square pyramid (see Fig. 13(a)). This is attributed to the larger interstice and the central stacked particle forcing the lower particles into a more circular arrangement. The spectra for the hexamer simulated via the FEM and the experimental spectra for these structures agree well with each another [144]. Fig. 13(d) shows the surface charge distribution at two peak wavelengths (585 and 705 nm), which responds to the coupling effect originating from the multipolar modes and dipole modes, respectively.

However, it is again worth emphasizing that any symmetry breaking will also introduce strong coupling between dark modes and bright modes, and the corresponding spectra will then change dramatically. Note that the magnetic mode also exists in the 3D tetramer and pentamer cluster. These symmetric 3D magnetic molecules are two-dimensionally isotropic and polarization-independent, which is extremely promising for constituting metamaterials with negative permeability [19], negative refractive index [17] and other plasmonic applications.

This assembly approach paves the way for the formation of more complex, functional, three-dimensional plasmonic assemblies, including chiral assemblies.

## Ageing of DNA assembled nanostructures

A common feature of all the structures assembled here using DNA is a change in the optical spectrum of the resulting assembly over a timescale of days to weeks. Fig. 14(a) shows the spectra of a 4-particle chain as a function of time after fabrication. During the first 5 days, the longitudinal band of the structure blue shifts by approximately 75 nm and a broadening of the transverse band is evident. Similar changes with time of the scattering spectra for dimers, 2D trimers, 2D tetramers and other linear chains were also observed: longitudinal bands blue shift, while transverse bands broaden and in some cases blue shift also. Despite these optical changes, no change in the structure of the assemblies were apparent from the SEM micrographs. Fig. 14(b) shows SEM images of the 4-particle chain when the structure was first fabricated (left) and 7 days later (right). We therefore conclude that the changes in the optical properties are due to gradual changes in the DNA/CTAB ligand layer. One possible cause is the slow dehydration of the DNA ligand layer, which could alter the refractive index immediately surrounding the nanoparticle assembly. This would lead to shifts in the SP resonance. Clearly the scattering spectra of assembled structures should be acquired immediately following assembly.

## Post synthetic modification

A new approach to the fabrication of functional metallic nanocrystalline particle arrays involves a combination of the top-down and bottom-up approaches to nanofabrication. It exploits the crystalline nature of chemically synthesized nanocrystals by using these as a precursor and then using a focussed ion-beam (FIB) milling to post-synthetically modify the crystal in some way. Using this technique, fabrication of flat crystalline structures with random shapes has been achieved [102] and the resulting structures show high quality optical properties [102,103].

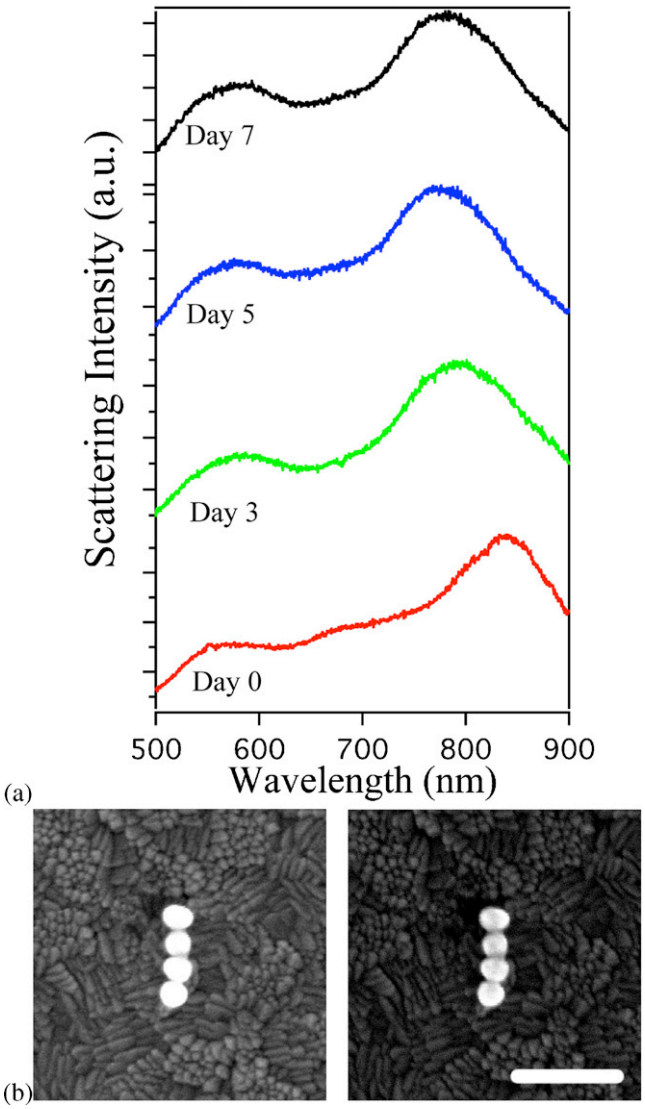


**Figure 14** (a) The spectra of a linear 4 particle chain taken when first fabricated (day 0) as well as 3 days, 5 days and 7 days after fabrication. Images of the 4 particle chain can be seen when the structure was first fabricated (left) and after 1 week (right). Scale bar = 250 nm.

In these reports, chemically synthesized large, microscale plates were used as the crystalline precursor to allow plate-like two dimensional structures of random shapes to be fabricated. Extending this approach by taking as the starting material nanoscale (in place of microscale) crystalline particles however allows nanoparticles with three-dimensional structure to be achieved. A longstanding goal of plasmonics researchers has been the fabrication of highly regular nanoparticle arrays in which the individual nanocrystals are crystalline [145,146]. This cannot be achieved by lithographic means at present, and whilst there has been some success via various modes of micromanipulation (for example with an AFM tip or similar form of micro-/nanomanipulation [145,147,148]), these approaches are highly time-consuming and are often limited to larger nanoparticles. Some progress has been made towards this

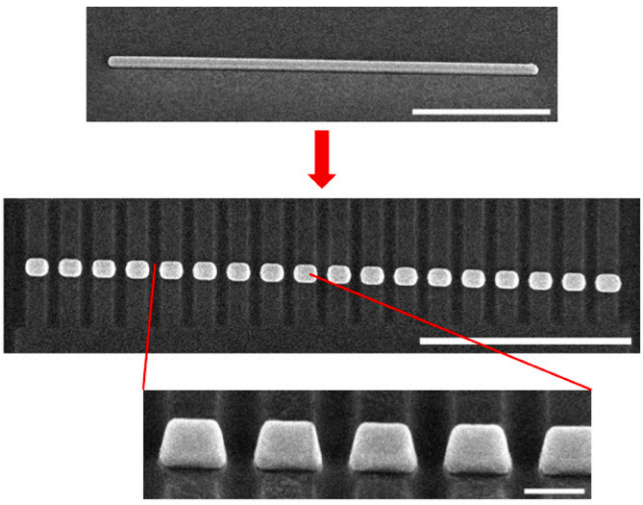

**Figure 15** Top: SEM image of a silver nanowire prior to FIB milling taken at 52° to the plane of the substrate. Middle: The nanoparticle array after FIB milling showing linear array of crystalline nanoparticles and shallow etch marks in the substrate. The fabricated linear Ag nanocrystal array contains 18 nanoparticles with average nanoparticle dimensions of: length 110 nm, width 84 nm, aspect ratio 1.3 and interparticle separation 52 nm. The total array length is 2.8 μm. Bottom: High resolution image showing the straight sides of the individual nanoparticles (taken at 52° to the plane of the substrate). Scale bar top and middle are 1000 nm, bottom 100 nm.

goal using the DNA-based assembly techniques outlined above [149]. However, the combination of the top-down and bottom-up approach to nanofabrication presents a unique opportunity to achieve this goal using a similar approach but one optimized for the formation of linear arrays of metal nanocrystals. In this case, the nanocrystal ''templates'' to be post-synthetically modified are chemically synthesized colloidal silver nanowires. The nanowires have a pentagonal cross-section, with a diameter ranging from around 40 nm up to around 140 nm depending on the synthetic conditions used and have lengths up to a few tens of microns [150—152]. The FIB milling of a number of regular ''cuts'' across and through the nanowire (perpendicular to its length) following its dispersion on a solid substrate leads to the fabrication of a number of discrete crystalline nanoparticles as shown in Fig. 15. The mill depth is set to ensure the nanowires are completely milled through to give a clean ''cut'' whilst minimizing damage to the substrate.

Using this approach, linear arrays of >50 nanocrystals spanning a length of >11 μm have been fabricated [153]. The dimensions, length and interparticle separation of the nanocrystals in the arrays are able to be controlled as is evident from the linear arrays shown in Fig. 16. This includes the control of the particle sizes, aspect ratios and interparticle separations. The interparticle separations in the arrays have been varied from 20 nm to 200 nm (Fig. 16(c)) and although much larger interparticle separations are possible, the degree of coupling at these longer distances becomes minimal. Generally, using nanowires of width 100 nm or less, the aspect ratio will be 1 or greater (when the width is taken as the width of the starting nanowire), giving rise to a nanoparticle array consisting of nanorods aligned end-to-end, a geometry which has been shown to display strong plasmon coupling [154]. The smallest separation achieved to date is 20 nm [153].

The fabricated arrays display a consistent interparticle separation as well as very high uniformity of the nanocrystal dimensions throughout the arrays. The standard deviations for the arrays are well within one pixel of the captured SEM image (even at higher SEM resolutions) generally approximately 2 nm or less. Thus there is less than 5 percent standard deviation in these dimensions. A slightly higher standard deviation (around 3 nm) was observed for particles fabricated in areas where the curvature of the original nanowire changed and where, as expected, the nanoparticle length changed slightly as a result. It is possible to account for the nanowire curvature and therefore minimize the standard deviation in particle dimensions across the array by an appropriate modification of the angle of the milled ''cuts'' to reflect the angle of curvature rather than keeping the milled lines perfectly parallel to one another. The uniformity of the nanocrystal dimensions makes these fabricated linear arrays of crystalline nanoparticles promising for applications within optoelectronics. The optical properties and potential waveguiding ability of these linear nanocrystal arrays are currently being investigated.

Another modality for the coupling of plasmon resonances of nanoparticles is the coupling between a core and shell with different dielectric constants. In this case, the plasmon dipole of the spherical shell couples to the plasmon supported within the cavity. It was this geometry for which the plasmon hybridization model was first reported and tested [155,156]. In contrast to the coupling between two nanoparticles, the higher symmetry of the one-dimensional coupling system leads to identical energy levels for both electromagnetic polarization states in the absence of a substrate effect [157—159], and so there are no dark modes [155,156]. The coupling between a core — or 'hole' and shell allows the modification of the particle plasmon resonance without changing the intrinsic shape of the particle but via the creation of a hole in the particle. A combination of the top-down and bottom-up approaches to the fabrication of nanoparticles outlined above allows the creation of holes in a single crystal particle via the milling of a hole using a focussed ion beam (FIB) in colloidally synthesized nanocrystals dispersed on a slide. Fig. 16(b) shows the SEM images of a single crystal trigonal prism and a hexagonal plate after the milling of a hole through the centre of each crystal using a FIB.

The above examples illustrate the power of the combined top-down and bottom-up method to create either individual nanoparticles or coupled nanoparticles with unique plasmonic properties.

## Chiral structures

The formation of plasmonic architectures which display strong optical chirality in the visible region is a significant advance in the field. This important goal has

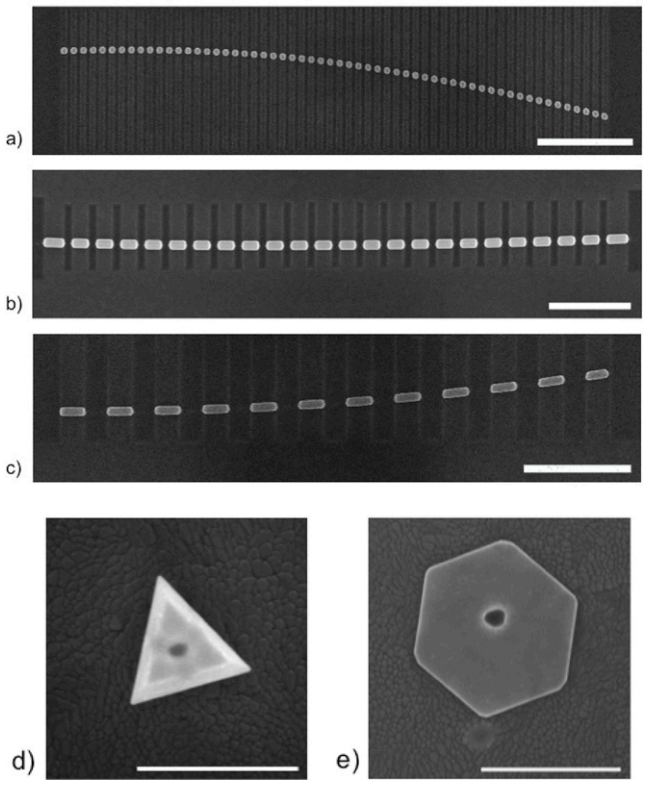


**Figure 16** (a) SEM images of different linear crystalline arrays of Ag nanoparticles fabricated using FIB milling. (a) Linear Ag nanocrystal array of 58 nanorods with total array length 5.8 μm and average nanoparticle dimensions of: length 67 nm, width 70 nm, aspect ratio 0.96 and interparticle separation 29 nm, scale bar 1000 nm. (b) Linear Ag nanocrystal array of 24 nanorods with total array length 7.2 μm and average nanoparticle dimensions of: length 220 nm, width 115 nm, aspect ratio 1.9 and interparticle separation 80 nm, scale bar 1000 nm. (c) Linear Ag nanocrystal array of 12 nanorods with total array length 5.2 μm and average nanoparticle dimensions of: length 250 nm, width 22 nm, aspect ratio 3.0 and interparticle separation 196 nm, scale bar 1000 nm. (d and e) SEM images of a trigonal prism (scale bar 400 nm) and a hexagonal plate (scale bar 500 nm), respectively with a hole milled through the centre of the nanocrystal.

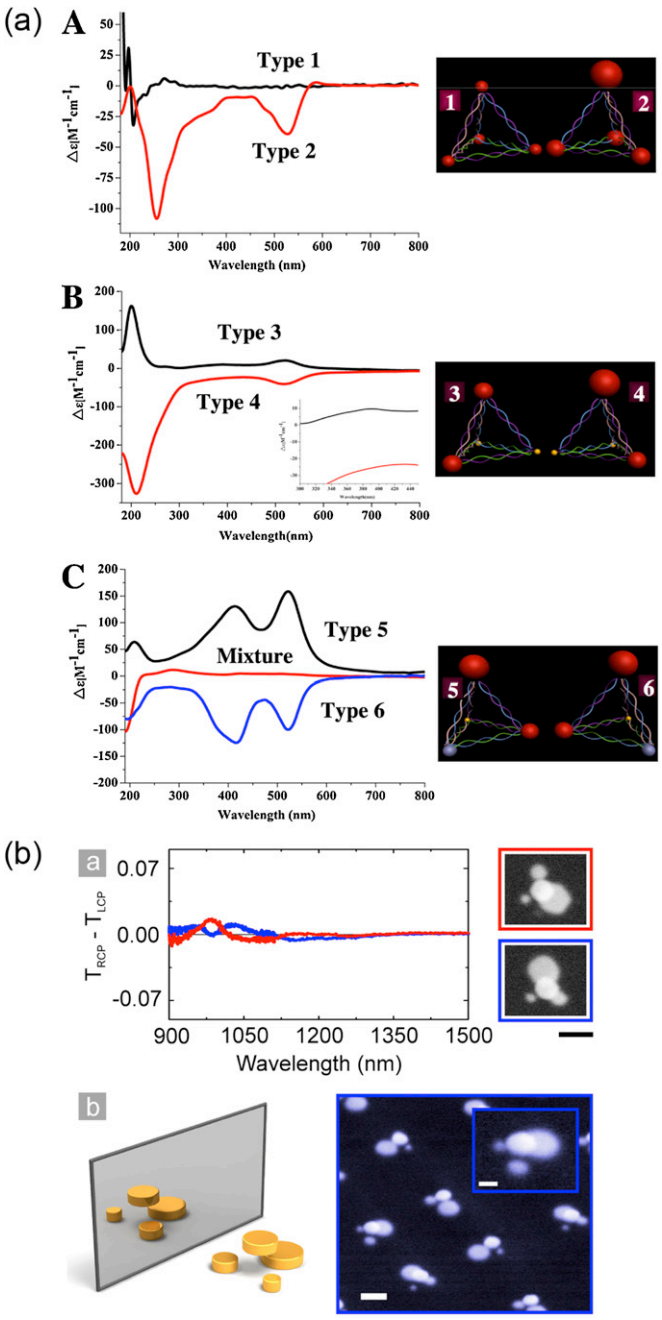


**Figure 17** (a) Circular dichroism spectra of self-assembled pyramids made from (A) four Au1 (type 1) and three Au2 + Au3 (type 2); (B) two Au2 + two QDs (type 3), and Au2 + Au3 + two QDs (type 4) [inset: CD spectrum in 300—450 nm region]; and (C) Au2 + Au3 + Ag + QD as S- (type 5) and R-enantiomers (type 6) [161]. (b) (above) Spectra and SEM close-up micrographs of compositionally chiral clusters. Scale bar is 200 nm. (b) Artist impression of the compositionally chiral clusters and tilted view SEM micrographs of the clusters. The scale bar is 100 nm for the close-up images and 200 nm for the overview [160].

recently been achieved by a number of researchers using both lithographic [160] and DNA self-assembly approaches [161,162].

A chiral plasmonic structure may be designed by incorporating nanoparticles of varying size, shape or material at each position within a structure complex enough to have a non-superimposable mirror image. Chiral enantiomers are then achieved by switching the positions of any two nanoparticles. Three-dimensional structures are required to achieve assemblies that interact differently with right- and left-handed circularly polarized light. The smallest chiral assemblies are based on a tetrahedral (or tetrahedra with intentionally broken symmetry) and these may be thought of as the building-blocks for the formation of highly chiral structures. Nanoparticle position [160], size [161] and material [161] variation of the individual nanoparticles in tetrahedral (or tetrahedral-based) assemblies have been shown to interact differently with right- and left-handed circularly polarized light, indicating the chirality present within these structures. Additionally, perfectly opposite CD spectra (in terms of

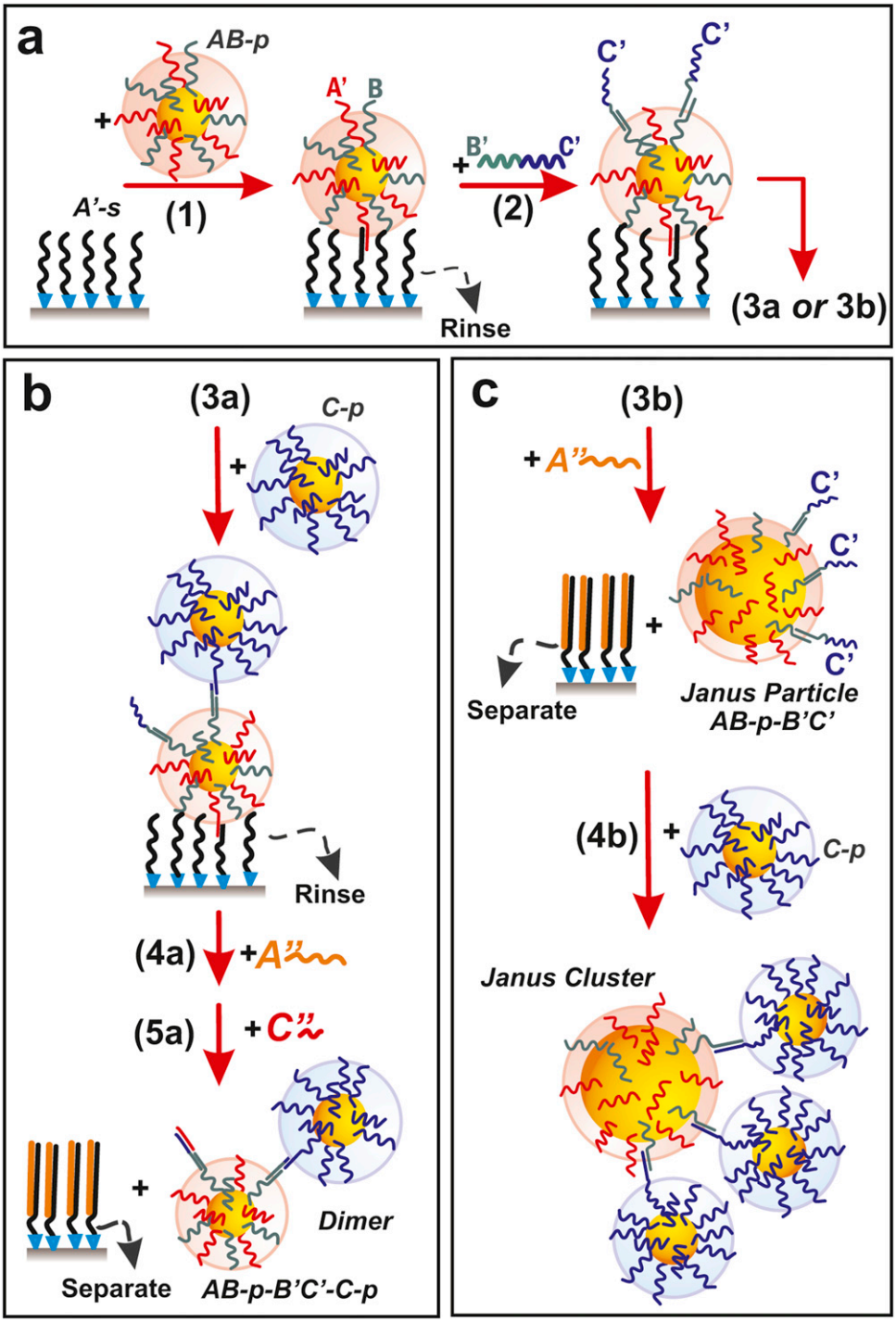


**Figure 18** The assembly and encoding steps in fabricating symmetric dimer nanoclusters or asymmetric Janus particles and clusters. (a) Surface encoding begins by grafting A′-ssDNA strands at paramagnetic bead supports (A′-s), followed by the immobilization of A- and B-ssDNA-functionalized particles (AB-p) through 15-bp A′A hybridization (step 1). After a purification step (rinse), facilitated by magnetic separation of the A′-s, the B′C′-l ssDNA linker is added, which recognizes only the AB-p through 15 bp BB′ hybirization (step 2). (b) Dimer nanoclusters can then be fabricated by the assembly of C-ssDNA-functionalized particles (C-p) through 18-bp C′C hybridization (step 3a). Next, the assembled dimers are released from the support by adding A″ fuels strands that recognize the A′-s through 23-bp A′A′prime; hybridization, thus replacing the A′A linkages. Finally, and free C′ recognition sites are passivated by adding C″ ssDNA (step 5a). (c) Alternatively, the immobilized particles from steps 1 and 2 (a) are released from A′-s (step 3b), thus forming Janus particles [165].

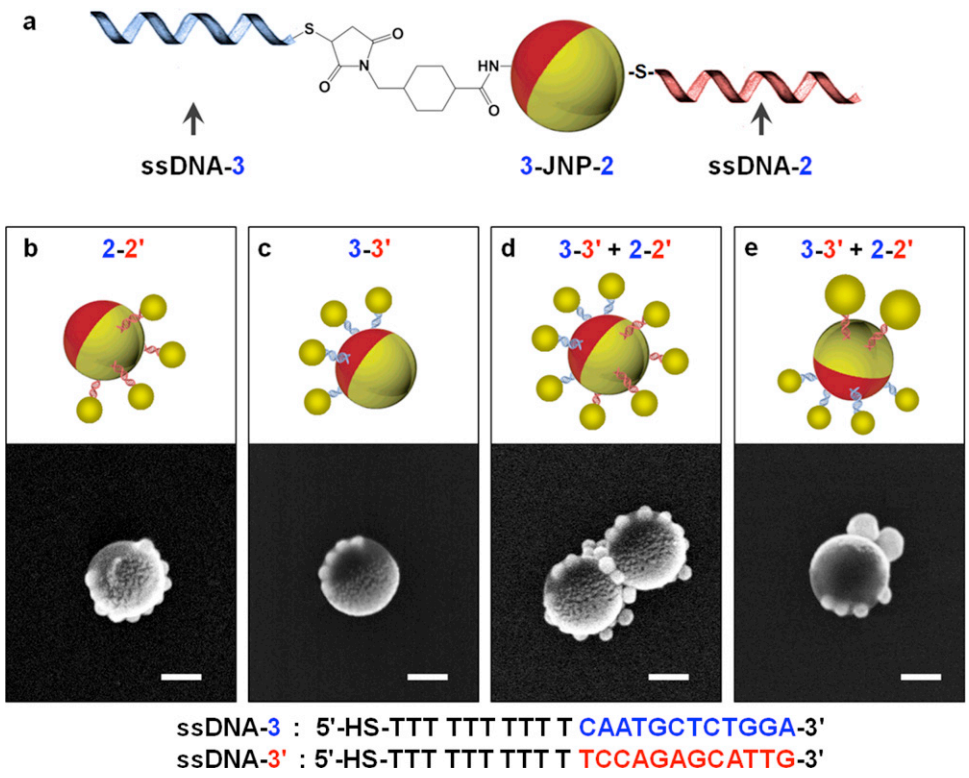


**Figure 19** (a) Schematic view of two different coupling chemistries on the surface of an amine-modified 200 nm Janus nanoparticles. (b—e) Schematic views and SEM images of representative asymmetric nanoclusters formed by dual DNA-functionalized Janus nanoparticles and different DNA-encoded gold nanoparticles: (b) 40 nm gold nanoparticle-20, (c) 40 nm gold nanoparticle-30, and (d) equal mixture of 40 nm gold nanoparticle-20 and gold nanoparticle-30; (e) equal mixture of 80 nm gold nanoparticle-20 and 40 nm gold nanoparticle-30 (scale bar = 100 nm) [168].

peak position and intensity) have been obtained from mirror images of the same structure — nominally labelled as the R- and S-enantiomers [160,161] as shown in Fig. 17(a and b).

A slightly different approach for the formation of chiral nanoparticle-based structures based the helicity (handedness) of double-stranded DNA is the attachment of small metal nanoparticles to helical DNA strands [162]. This approach results in right- or left-handed (depending on the initial DNA conformation) helices of nanoparticles with somewhat random spacing. The helical arrangement of the nanostructures results in coupled plasmon modes propagating along a helical path, causing an increased absorption of the components of the incident light in accord with the handedness of the helices, confirmed via ensemble CD measurements. Helical arrangements with left-handed chirality show CD spectra with a peak-dip line-shape and right-handed helices produce a vertically mirrored spectrum. Plasmonic interactions between the individual gold particles within each helix creates a splitting between the longitudinal and transverse modes of the electromagnetic wave, and these modes typically have opposite chirality. As a result, the plasmonic CD spectrum acquires the characteristic dip-peak shape [162].

The assembly of plasmonic structures with chiral optical properties has potential to allow for the creation of optical metamaterials. The achievement of structures with chiral optical characteristics illustrates the very specific control possible utilizing DNA-based assemblies.

## Larger plasmonic architectures

The next step in DNA self-assembly of metal nanoparticles is to incorporate these discrete structures into larger plasmonic architectures. The major hurdle is the poor yields associated with DNA assembly. This can be improved with purification via gel electrophoresis although it has only been used for structures where only 1 DNA strand per particle is required. More complex plasmonic structures will require more than 1 DNA strand per particle to allow for multi-functional building blocks for DNA based assemblies.

Assembly methods lacking specific directional control of the nanoparticles, such as the three-dimensional assembly of Au nanospheres into superstructures reported to date [163,164] result invariably in the formation of close-packed or cubic structures with interparticle separation controlled only by the ligand shell. In order to achieve the flexibility required for useful and specific incorporation of plasmonic structures into useful devices, greater control over the repeat unit is required. Progress has been made in this area by the anisotropic DNA functionalization of nanoparticles

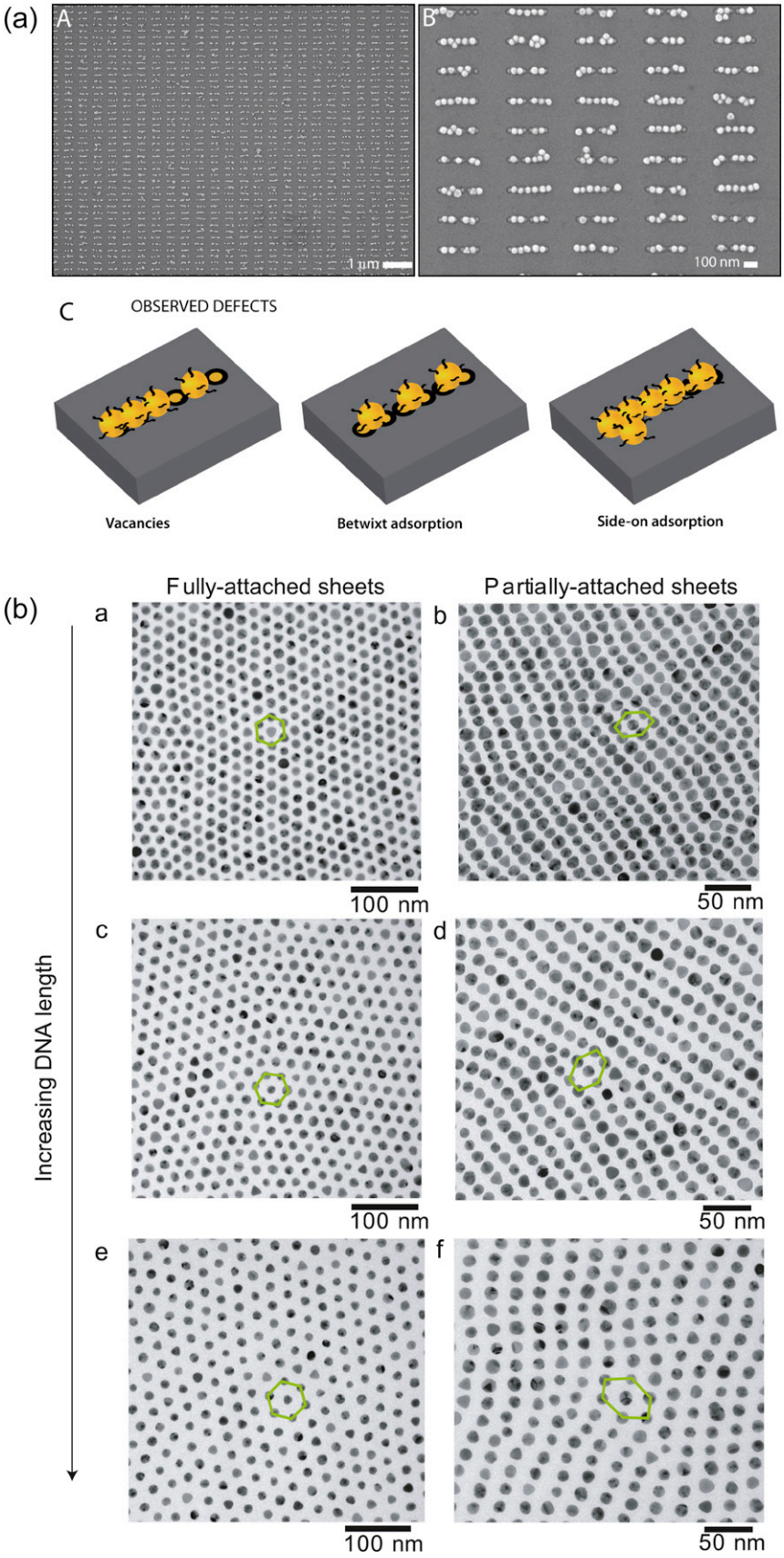


**Figure 20** (a) SEM micrographs and schemes of a substrate following the AuNP self-assembly process and schematic illustrations of observed defects in assembly configurations from Lalander et al. [170]. (b) Nanospheres assembled using DNA sheets. Reproduced from Chen et al. [54].

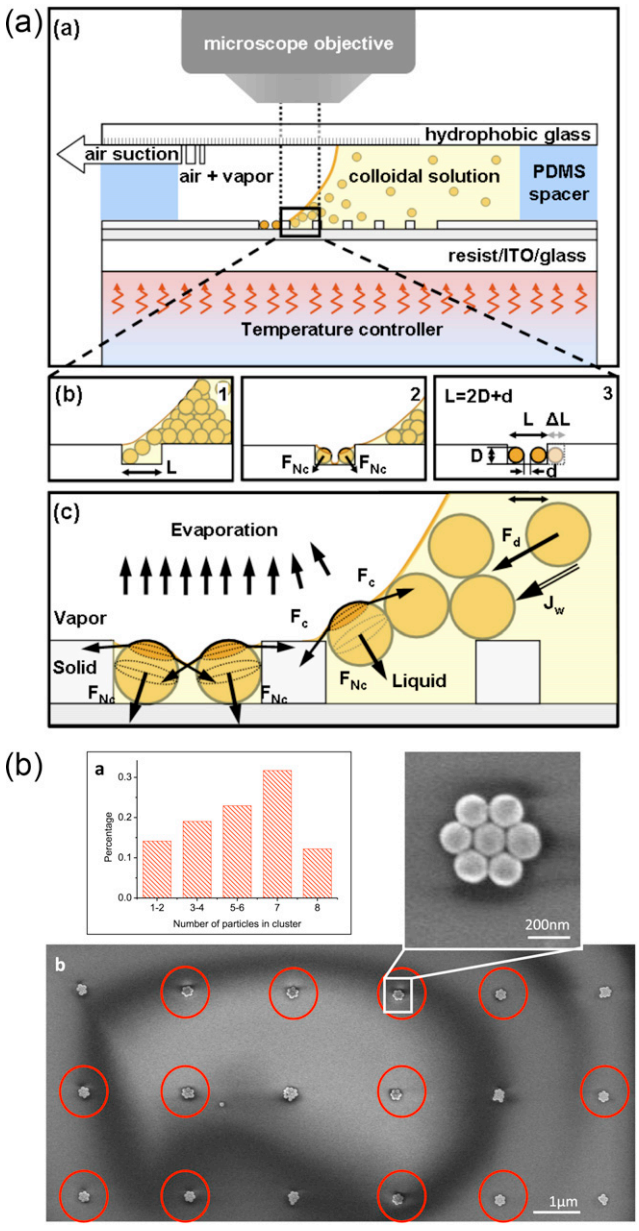


**Figure 21** Above: (a) Schematic description of the convective-CFA set-up for the fabrication of dimeric objects. (b) Sketch of the principle of dimer fabrication by capillary separation. L is the pattern's longest dimension, D is the colloids diameter and d is the edge-to-edge spacing between particles. (c) Hydrodynamic (Fd) and capillary (Fc and FNc) forces exerted on colloids at the triple contact-line and the capillary forces responsible for colloids separation in a template. Reproduced from Rivera et al. [171]. Below: Image of heptamers assembled using the convective-CFA technique. (a) Histogram of the distribution of clusters assembled on the PDMS template. Heptamers are assembled with 32% yield. (b) SEM image of an array of heptamers assembled on a PDMS template. The heptamers are circled; other types of clusters also are visible due to the stochastic nature of the assembly process. The inset shows a detailed image of an individual heptamer. Reproduced from the work of Fan et al. [174].

where the nanoparticles are grafted to a substrate, blocking one side of each individual particle [165—167]. Only the exposed side of the particle is then presented for functionalization with either DNA or another functional molecule. Following functionalization, the grafts are cleaved, resulting in Janus, or two-faced nanoparticles (see Fig. 18). Dimer yields as high as 73% have been reported using this surface encoding method [165]. A natural extension of this method would be the synthesis of nanoparticles with different DNA strands on either side of the nanoparticles (as opposed to one type of strand on one side) increasing the degree of directionality imparted to any resultant assembly. To this end, partially coated gold:polystyrene Janus nanoparticles have been shown to achieve two-sided anisotropic functionalization (see Fig. 19) [168]. These techniques, used in conjunction with purification techniques, could lead to bimodified nanoparticles, resulting in high yields of linear chain structures [169]. Controlling the angle between the placements of each DNA strand as well as decreasing the area functionalized by each DNA strand is the next hurdle in this area of research.

The specific placement of the assembled discrete plasmonic nanostructures on a substrate is also a necessary requirement to form functional plasmonic circuits. This is by no means a trivial task as coating nanoparticle solutions onto a substrate introduces capillary forces that can alter nanostructure geometries if not anticipated. To this end, via the use of lithographic templates, DNA-directed self assembly of individual building blocks (in this case, single gold nanospheres) has been achieved [170]. Using an etching, evaporation and lift-off process involving electron beam lithography (EBL) nanopatterns consisting of 6-dot line structures of gold were created on a silicon substrate, with each dot being 36 nm in diameter. These gold patterns were then functionalized with DNA. Gold nanospheres of 40 nm diameter and functionalized with the complementary DNA strands were assembled into the 6-dot line structures, resulting in chains of assembled nanospheres. The results of this assembly approach can be seen in Fig. 20. Fig. 20(a and b) shows SEM images of a typical assembly, and it can be seen that the yield is relatively low, with only 4 of the 45, or 8.9% of the structures shown in Fig. 20(b) reflecting the structure of the underlying nanopattern array. The low yield is attributed to three defect types that are possible in this assembly process: vacancies, betwixt adsorption and side-on adsorption (Fig. 20(c)).

The manipulation of capillary forces is an alternative method for spatially directing discrete plasmonic structures onto a templated substrate. Via the utilization of convective-capillary force assembly in conjunction with the capillary separation effect, nanoparticle dimers have been fabricated with 150 nm diameter gold particles with controlled interparticle separations between 0 and 230 nm [171]. The technique is based on the regulation of convective hydrodynamic and capillary immersion forces during the evaporation of a colloidal dispersion by two external parameters: temperature ($T$) and air-suction flow rate ($Q$) (Fig. 21(a and c)). By controlling these two forces, the motion of the nanoparticles can be driven towards the contact-line so as to increase the assembly

efficiency. The spacing between the particles in dimeric colloidal objects is modulated by the capillary separation effect that occurs when solvent evaporates within a template (Fig. 21(b and c)). Consequently, the edge-to-edge spacing between two colloid particles can be geometrically modulated by adjusting the template size to the colloids diameter as shown in Fig. 21(b). In addition to nanoparticle dimers [171,172], nanoparticle chains [173] and other two-dimensional arrays [173,174] (see Fig. 21) have also been assembled. An interesting variation on this was presented by Cheng and colleagues [175] (see Fig. 20), who created free standing, gold nanorod monolayer arrays with DNA as spacers. The method exploited the alignment induced by holes in a film. This is reminiscent of the original work on 2D arrays first published by Giersig almost 20 years ago [26] and highlights the incredible improvements in our understanding of the forces involved in self-assembly and how DNA can assist in the preparation of more sophisticated and tailored nanocrystal superlattices.

## Current, future directions and conclusion

Self-assembly, whilst still an area in its infancy, continues to have profound effects on the field of nanoparticle plasmonics. Although there are many methods for assembling metallic nanoparticles, each with their own benefits and drawbacks, DNA self-assembly has proved to be the most versatile method to date for creating nanostructures of varying complexity and design. DNA self-assembly has allowed a greater understanding of the ways that plasmons couple in nanoparticle structures. It is a powerful method for the fabrication of plasmonic assemblies and has allowed significant progress towards the assembly of nanocrystals into discrete structures with useful optical properties. Along with this progress, a number of challenges remain. For nanocrystal systems, the yields for formation of the desired structures are still relatively low, even for highly complex and specific hybridization schemes. Realistically, in order to make full use of the assembled structures in optical applications, either the preparation or purification of the desired structure to remove unwanted structures (higher and lower order assemblies) must be improved, and gel electrophoresis employed by some groups goes a significant way towards this. It is also clear from the results shown here that careful thought must be given to the constituent nanoparticle size and DNA oligomer length to obtain the desired nanoparticle spacings of the structure on the substrate. Smaller nanocrystals generally give an interparticle spacing closer to that predicted from the DNA oligomer length, and this is again improved by the use of longer DNA oligomers. However, smaller nanocrystal structures are generally more difficult to interrogate using stand optical means (in particular light scattering) and despite these general rules there is still considerable variation in the obtained interparticle separation. Conversely, the use of larger nanocrystals will tend to produce structures in which the individual nanoparticles are in primary ligand contact, complicating the modelling for these assemblies. It is only with very careful consideration of the van der Waals attraction between particles vs DNA length that interparticle separations in the 1—4 nm range be achieved and it is likely that assemblies that achieve this will only be able to be fabricated with smaller nanocrystals.

The optical properties of the assemblies created by DNA-directed self-assembly are complex. They may be used as a means to evaluate the symmetry of the structures created. We group them here into a number of different classes which display commonalities in their optical responses — one-dimensional linear arrays, two-dimensional, cyclic structures and three-dimensional structures. The coupling of linear arrays of nanoparticles may provide a means for the transport of an optical signal via waveguiding. The gradual asymptotic red-shift of the optical signal when the incoming electric field is oriented parallel to the chain axis observed for the linear chains is characteristic of a system able to guide light. The strong-coupling regime obtained by the DNA-directed assembly for the arrays potentially also leads to subradiant modes which are predicted to be low-loss. However, for direct observation of waveguiding, longer chains and chains with variable interparticle separation are required. Whilst the top-down/bottom up fabrication combination can achieve longer arrays, the interparticle separation is normally around 20 nm. For perfectly cyclic structures, the optical response is generally highly polarization-independent for in-plane excitation; however the lowest energy dark, magnetic (cyclic) mode contributes considerably to the optical response if the structure is even slightly asymmetric, leading to the formation of Fano-like modes. These modes are of particular interest in SERS sensing. The addition of nanocrystals to the interstices of a cyclic structure results in the formation of a three-dimensional structure and these can be built up on a substrate in a stepwise manner. Further extension of this technique has the potential to create larger, yet still discrete three-dimensional structures. The tetrahedra created and shown here using this technique are particularly notable due to their completely polarization-independent optical response.

Significant progress has been made in the assembly of discrete nanocrystal assemblies using DNA. Further challenges in the field include the incorporation of the structures into useful devices via either specific or regular placement of the structures onto a substrate and their combination with other elements, including for example, quantum dots or graphene. A particularly important further goal in the field of nanocrystal self-assembly is the assembly of the individual structures formed into higher order, continuous structures, in both two- and three-dimensions. The alternative top-down/bottom up FIB-based fabrication provides a means for the specific placement of, for example, a linear array on a substrate on a very small scale for proof-of-principle measurements via the micromanipulation of the starting colloid. The continued development and improvement of assembly methods is paramount to achieving these aims and therefore further significant progress in this field.

## Acknowledgements

This work was supported through ARC Grants LF100100161 and FT110100545. S.J.B. would like to thank the

University of Melbourne for the Ernst and Grace Matthaei research scholarship. The authors thank Sergey Rubanov for assistance with FIB/SEM at Bio21, The University of Melbourne. This work was performed in part at the Melbourne Centre for Nanofabrication.

## Appendix A. Supplementary data

Supplementary data associated with this article can be found, in the online version, at http://dx.doi.org/10.1016/j.nantod.2013.02.005.

## References

[1] C. Eggeling, J. Schaffer, C.A.M. Seidel, J. Korte, G. Brehm, S. Schneider, et al., J. Phys. Chem. A 105 (2001) 3673—3679.
[2] D.-K. Lim, K.-S. Jeon, H.M. Kim, J.-M. Nam, Y.D. Suh, Nat. Mater. 9 (9) (2010) 60—67.
[3] Y. Fu, J. Zhang, J.R. Lakowicz, J. Am. Chem. Soc. 132 (2010) 5540—5541.
[4] F.F. Lu, T. Li, J. Xu, Z.D. Xie, L. Li, S.N. Zhu, et al., Opt. Express 19 (2011) 2858—2865.
[5] N. Yu, J. Fan, Q.J. Wang, C. Pflugl, L. Diehl, T. Edamura, et al., Nat. Photon. 2 (2008) 564—570.
[6] D.B. Shao, S.C. Chen, Appl. Phys. Lett. 86 (2005), 253107-253107-3.
[7] S. Pillai, K.R. Catchpole, T. Trupke, M.A. Green, J. Appl. Phys. 101 (2007), 093105-093105-8.
[8] E. Kowalska, O.O.P. Mahaney, R. Abe, B. Ohtani, Phys. Chem. Chem. Phys. 12 (2010) 2344—2355.
[9] B.M. Reinhard, S. Sheikholeslami, A. Mastroianni, A.P. Alivisatos, J. Liphardt, Proc. Natl. Acad. Sci. U.S.A. 104 (2007) 2667—2672.
[10] K.M. Mayer, S. Lee, H. Liao, B.C. Rostro, A. Fuentes, P.T. Scully, et al., ACS Nano 2 (2008) 687—692.
[11] T. Endo, K. Kerman, N. Nagatani, H.M. Hiepa, D.K. Kim, Y. Yonezawa, et al., Anal. Chem. 78 (2006) 6465—6475.
[12] C.X. Yu, Irudayaraj, J. Anal. Chem. 79 (2007) 572—579.
[13] A.J. Haes, R.P. Van Duyne, J. Am. Chem. Soc. 124 (2002) 10596—10604.
[14] S.A. Maier, M.L. Brongersma, P.G. Kik, S. Meltzer, A.A.G. Requicha, H.A. Atwater, Adv. Mater. 13 (2001) 1501—1505.
[15] S.A. Maier, P.G. Kik, H.A. Atwater, Appl. Phys. Lett. 81 (2002) 1714—1716.
[16] V.K. Valev, A.V. Silhanek, B. De Clercq, W. Gillijns, Y. Jeyaram, X. Zheng, et al., Small 7 (2011) 2573—2576.
[17] V.M. Shalaev, Nat. Photon. 1 (2007) 41—48.
[18] A. Alu, N. Engheta, Opt. Express 17 (2009) 5723—5730.
[19] A. Alu, A. Salandrino, N. Engheta, Opt. Express 14 (2006) 1557—1567.
[20] C. Bohren, D. Huffman, Absorption and Scattering of Light by Small Particles, in: Wiley Science Paperback Series, 1st ed., Wiley Science, New York, 1998.
[21] U. Kreibig, M. Vollmer, Optical Properties of Metal Clusters, vol. 25, 1st ed., Springer, New York, 1995.
[22] D.A. Weitz, M. Oliveria, Phys. Rev. Lett. 52 (1984) 1433—1436.
[23] B.L.V. Prasad, C.M. Sorensen, K. Klabunde, J. Chem. Soc. Rev. 37 (2008) 1871—1883.
[24] C.D. Bain, G.M. Whitesides, J. Am. Chem. Soc. 111 (1989) 7164—7175.
[25] E.B. Troughton, C.D. Bain, G.M. Whitesides, R.G. Nuzzo, D.L. Allara, M.D. Porter, Langmuir 4 (1988) 365—385.
[26] M. Giersig, P. Mulvaney, Langmuir 9 (1993) 3408—3413.
[27] T. Jain, F. Westerlund, E. Johnson, K. Moth-Poulsen, T. Bjornholm, ACS Nano 3 (2009) 828—834.
[28] S.T.S. Joseph, B.I. Ipe, P. Pramod, K.G. Thomas, J. Phys. Chem. B 110 (2006) 150—157.
[29] F. Westerlund, T. Bjornholm, Curr. Opin. Colloid Interface Sci. 14 (2009) 126—134.
[30] M. Sethi, G. Joung, M.R. Knecht, Langmuir 25 (2009) 1572—1581.
[31] I.E. Sendroiu, S.F.L. Mertens, D. Schiffrin, J. Phys. Chem. Chem. Phys. 8 (2006) 1430—1436.
[32] K.G. Thomas, S. Barazzouk, B.I. Ipe, S.T.S. Joseph, P.V. Kamat, J. Phys. Chem. B 108 (2004) 13066—13068.
[33] C.S. Weisbecker, M.V. Merritt, G.M. Whitesides, Langmuir 12 (1996) 3763—3772.
[34] K.K. Caswell, C.J. Murphy, J.N. Wilson, U.H.F. Bunz, J. Am. Chem. Soc. 125 (2003) 13914—13915.
[35] C.A. Mirkin, R.L. Letsinger, R.C. Mucic, J.J. Storhoff, Nature 382 (1996) 607—609.
[36] C. Sonnichsen, B.M. Reinhard, J. Liphardt, A.P. Alivisatos, Nat. Biotechnol. 23 (2005) 741—745.
[37] F.A. Aldaye, H.F. Sleiman, Angew. Chem. Int. Ed. 45 (2006) 2204—2209.
[38] F.A. Aldaye, H.F. Sleiman, J. Am. Chem. Soc. 129 (2007) 4130—4131.
[39] E. Dujardin, L.B. Hsin, C.R.C. Wang, S. Mann, Chem. Commun. (2001) 1264—1265.
[40] B.F. Pan, L.M. Ao, F. Gao, H.Y. Tian, R. He, D.X. Cui, Nanotechnology 16 (2005) 1776—1780.
[41] H. Yao, C.Q. Yi, C.H. Tzang, J.J. Zhu, M.S. Yang, Nanotechnology 18 (2007) 1—7.
[42] Y.X. Zhang, H.C. Zeng, J. Phys. Chem. B 110 (2006) 16812—16815.
[43] J.W. Zheng, P.E. Constantinou, C. Micheel, A.P. Alivisatos, R.A. Kiehl, N.C. Seeman, Nano Lett. 6 (2006) 1502—1504.
[44] H. Katz-Boon, C.J. Rossouw, M. Weyland, A.M. Funston, P. Mulvaney, J. Etheridge, Nano Lett. 11 (2011) 273—278.
[45] E. Carbo-Argibay, B. Rodriguez-Gonzalez, S. Gomez-Grana, A. Guerrero-Martnez, I. Pastoriza-Santos, J. Perez-Juste, et al., Angew. Chem. Int. Ed. 49 (2010) 9397—9400.
[46] A.J. Mastroianni, S.A. Claridge, A.P. Alivisatos, J. Am. Chem. Soc. 131 (2009) 8455—8459.
[47] J.A. Fan, Y. He, K. Bao, C. Wu, J. Bao, N.B. Schade, et al., Nano Lett. 11 (2011) 4859—4864.
[48] S. Sheikholeslami, Y.W. Jun, P.K. Jain, A.P. Alivisatos, Nano Lett. 10 (2010) 2655—2660.
[49] S. Barrow, A. Funston, D. Gomez, T. Davis, P. Mulvaney, Nano Lett. 11 (2011) 4180—4187.
[50] C.J. Loweth, W.B. Caldwell, X. Peng, A.P. Alivisatos, P.G. Schultz, Angew. Chem. Int. Ed. 38 (1999) 1808—1812.
[51] S. Pal, Z. Deng, B. Ding, H. Yan, Y. Liu, Angew. Chem. Int. Ed. 49 (2010) 2700—2704.
[52] B. Ding, Z. Deng, H. Yan, S. Cabrini, R.N. Zuckermann, J. Bokor, J. Am. Chem. Soc. 132 (2010) 3248—3249.
[53] Z. Deng, Y. Tian, S.-H. Lee, A.E. Ribbe, C. Mao, Angew. Chem. Int. Ed. 44 (2005) 3582—3585.
[54] W. Cheng, M.J. Campolongo, J.J. Cha, S.J. Tan, C.C. Umbach, D.A. Muller, D. Luo, Nat. Mater. 8 (2009) 519—525.
[55] R.C. Mucic, J.J. Storhoff, C.A. Mirkin, R.L. Letsinger, J. Am. Chem. Soc. 120 (1998) 12674—12675.
[56] A.P. Alivisatos, K.P. Johnsson, X. Peng, T.E. Wilson, C.J. Loweth, M.P. Bruchez, et al., Nature 382 (1996) 609—611, 10.1038/382609a0.
[57] N.C. Seeman, Biochemistry 42 (2003) 7259—7269.
[58] J.J. Storhoff, R. Elghanian, R.C. Mucic, C.A. Mirkin, R.L. Letsinger, J. Am. Chem. Soc. 120 (1998) 1959—1964.

[59] J.-Y. Kim, J.-S. Lee, Nano Lett. 9 (2009) 4564—4569.
[60] R.C. Jin, G.S. Wu, Z. Li, C.A. Mirkin, G.C. Schatz, J. Am. Chem. Soc. 125 (2003) 1643—1654.
[61] R. Sardar, A.M. Funston, P. Mulvaney, R.W. Murray, Langmuir 25 (2009) 13840—13851.
[62] D. Boyer, P. Tamarat, A. Maali, B. Lounis, M. Orrit, Science 297 (2002) 1160—1163.
[63] H. Staleva, G.V. Hartland, Adv. Funct. Mater. 18 (2008) 3809—3817.
[64] A. Arbouet, D. Christofilos, N.D. Fatti, F. Valle, J.R. Huntzinger, L. Arnaud, et al., Phys. Rev. Lett. 93 (2004) 127401.
[65] T. Klar, M. Perner, S. Grosse, G. von Plessen, W. Spirkl, Feldmann, J. Phys. Rev. Lett. 80 (1998) 4249—4252.
[66] C. Sonnichsen, S. Geier, N.E. Hecker, G. von Plessen, J. Feldmann, H. Ditlbacher, et al., Appl. Phys. Lett. 77 (2000) 2949—2951.
[67] C. Novo, D. Gomez, J. Prez-Juste, Z. Zhang, H. Petrova, M. Reismann, et al., Phys. Chem. Chem. Phys. 8 (2006) 3540—3546.
[68] M. Hu, C. Novo, A. Funston, H.N. Wang, H. Staleva, S.L. Zou, et al., J. Mater. Chem. 18 (2008) 1949—1960.
[69] P. Billaud, J.-R. Huntzinger, E. Cottancin, J. Lerme, M. Pellarin, L. Arnaud, et al., Eur. Phys. J. D 43 (2007) 271—275.
[70] C. Novo, A.M. Funston, I. Pastoriza-Santos, L.M. Liz-Marzan, P. Mulvaney, Angew. Chem. Int. Ed. 46 (2007) 3517—3520.
[71] M. Hu, J.Y. Chen, M. Marquez, Y.N. Xia, G.V. Hartland, J. Phys. Chem. C 111 (2007) 12558—12565.
[72] R.C. Jin, J.E. Jureller, H.Y. Kim, N.F. Scherer, J. Am. Chem. Soc. 127 (2005) 12482—12483.
[73] C.L. Nehl, N.K. Grady, G.P. Goodrich, F. Tam, N.J. Halas, J.H. Hafner, Nano Lett. 4 (2004) 2355—2359.
[74] P. Billaud, S. Marhaba, E. Cottancin, L. Arnaud, G. Bachelier, C. Bonnet, et al., J. Phys. Chem. C 112 (2008) 978—982.
[75] A.-I. Henry, J.M. Bingham, E. Ringe, L.D. Marks, G.C. Schatz, R.P.V. Duyne, J. Phys. Chem. C 115 (2011) 9291—9305.
[76] J. Rodriguez-Fernandez, A.M. Funston, J. Perez-Juste, R.A. Alvarez-Puebla, L.M. Liz-Marzan, P. Mulvaney, Phys. Chem. Chem. Phys. 11 (2009) 5909—5914.
[77] J. Rodriguez-Fernandez, C. Novo, V. Myroshnychenko, A.M. Funston, A. Sanchez-Iglesias, I. Pastoriza-Santos, et al., J. Phys. Chem. C 113 (2009) 18623—18631.
[78] C. Novo, A.M. Funston, A.K. Gooding, P. Mulvaney, J. Am. Chem. Soc. 131 (2009) 14664—14666.
[79] C. Novo, A.M. Funston, P. Mulvaney, Nat. Nanotechnol. 3 (2008) 598—602.
[80] E. Hao, G.C. Schatz, J. Chem. Phys. 120 (2004) 357—366.
[81] Y. Fang, N.-H. Seong, D.D. Dlott, Science 321 (2008) 388—392.
[82] E.J. Blackie, E.C.L. Ru, P.G. Etchegoin, J. Am. Chem. Soc. 131 (2009) 14466—14472.
[83] K. Kneipp, H. Kneipp, J. Kneipp, Acc. Chem. Res. 39 (2006) 443—450.
[84] A.D. McFarland, R.P. Van Duyne, Nano Lett. 3 (2003) 1057—1062.
[85] L. Rodriguez-Lorenzo, R.A. Alvarez-Puebla, I. Pastoriza-Santos, S. Mazzucco, O. Stephan, M. Kociak, et al., J. Am. Chem. Soc. 131 (2009) 4616—4618.
[86] V. Myroshnychenko, J. Rodriguez-Fernandez, I. Pastoriza-Santos, A.M. Funston, C. Novo, P. Mulvaney, et al., Chem. Soc. Rev. 37 (2008) 1792—1805.
[87] N.J. Halas, S. Lal, W.-S. Chang, S. Link, P. Nordlander, Chem. Rev. 111 (2011) 3913—3961, http://dx.doi.org/10.1021/cr200061k.
[88] M. Hentschel, M. Saliba, R. Vogelgesang, H. Giessen, A.P. Alivisatos, N. Liu, Nano Lett. 10 (2010) 2721—2726.
[89] T. Atay, J.H. Song, A.V. Nurmikko, Nano Lett. 4 (2004) 1627—1631.
[90] P.K. Jain, W.Y. Huang, M.A. El-Sayed, Nano Lett. 7 (2007) 2080—2088.
[91] W. Rechberger, A. Hohenau, A. Leitner, J.R. Krenn, B. Lamprecht, F.R. Aussenegg, Opt. Commun. 220 (2003) 137—141.
[92] K.H. Su, Q.H. Wei, X. Zhang, J.J. Mock, D.R. Smith, S. Schultz, Nano Lett. 3 (2003) 1087—1090.
[93] W. Huang, W. Qian, P.K. Jain, M.A. El-Sayed, Nano Lett. 7 (2007) 3227—3234.
[94] L. Gunnarsson, T. Rindzevicius, J. Prikulis, B. Kasemo, M. Kall, S.L. Zou, et al., J. Phys. Chem. B 109 (2005) 1079—1087.
[95] P.K. Jain, K.S. Lee, I.H. El-Sayed, M.A. El-Sayed, J. Phys. Chem. B 110 (2006) 7238—7248.
[96] A.M. Funston, C. Novo, T.J. Davis, P. Mulvaney, Nano Lett. 9 (2009) 1651—1658.
[97] P.K. Jain, M.A. El-Sayed, J. Phys. Chem. C 112 (2008) 4954—4960.
[98] P. Nordlander, C. Oubre, E. Prodan, K. Li, M.I. Stockman, Nano Lett. 4 (2004) 899—903.
[99] I. Romero, J. Aizpurua, G.W. Bryant, F.J.G.D. Abajo, Opt. Exp. 14 (2006) 9988—9999.
[100] J. Zuloaga, E. Prodan, P. Nordlander, Nano Lett. 9 (2009) 887—891.
[101] B.N. Khlebtsov, N.G. Khlebtsov, J. Phys. Chem. C 111 (2007) 11516—11527.
[102] J.-S. Huang, V. Callegari, P. Geisler, C. Bruning, J. Kern, J.C. Prangsma, et al., Nat. Commun. 1 (2010) 150.
[103] F.M. Huang, J.J. Baumberg, Nano Lett. 10 (2010) 1787—1792.
[104] H. Ditlbacher, A. Hohenau, D. Wagner, U. Kreibig, M. Rogers, F. Hofer, et al., Phys. Rev. Lett. 95 (2005) 4.
[105] B.J. Wiley, D.J. Lipomi, J.M. Bao, F. Capasso, G.M. Whitesides, Nano Lett. 8 (2008) 3023—3028.
[106] S. Marhaba, G. Bachelier, C. Bonnet, M. Broyer, E. Cottancin, N. Grillet, et al., J. Phys. Chem. C 113 (2009) 4349—4356.
[107] H. Tamaru, H. Kuwata, H.T. Miyazaki, K. Miyano, Appl. Phys. Lett. 80 (2002) 1826—1828.
[108] E. Prodan, C. Radloff, N.J. Halas, P. Nordlander, Science 302 (2003) 419—422.
[109] B.M. Reinhard, M. Siu, H. Agarwal, A.P. Alivisatos, J. Liphardt, Nano Lett. 5 (2005) 2246—2252.
[110] J. Prikulis, F. Svedberg, M. Kall, J. Enger, K. Ramser, M. Goksor, et al., Nano Lett. 4 (2004) 115—118.
[111] M.-W. Chu, V. Myroshnychenko, C.H. Chen, J.-P. Deng, C.-Y. Mou, F.J.G.D. Abajo, Nano Lett. 9 (2009) 399—404.
[112] S. Zhang, D.A. Genov, Y. Wang, M. Liu, X. Zhang, Phys. Rev. Lett. 101 (2008) 047401.
[113] T.J. Davis, K.C. Vernon, D.E. Gomez, Phys. Rev. B 79 (2009) 10.
[114] B. Willingham, S. Link, Opt. Express 19 (2011) 6450—6461.
[115] B. Luk'yanchuk, N.I. Zheludev, S.A. Maier, N.J. Halas, P. Nordlander, H. Giessen, et al., Nat. Mater. 9 (2010) 707.
[116] S.A. Maier, Plasmonics: Fundamentals and Applications, Springer Science, New York, 2007.
[117] T.J. Davis, D.E. Gomez, K.C. Vernon, Nano Lett. 10 (2010) 2618—2625.
[118] C. Pecharroman, J. Perez-Juste, G. Mata-Osoro, L.M. Liz-Marzan, P. Mulvaney, Phys. Rev. B 77 (2008) 035418.
[119] A. Funston, T.J. Davis, C. Novo, P. Mulvaney, Phil. Trans. R. Soc. A 369 (2011) 3472—3482.
[120] V.H.D.C. Tabor, M.A. El-Sayed, ACS Nano 3 (2009) 3670—3678.
[121] L. Shao, K.C. Woo, H. Chen, Z. Jin, J. Wang, H.-Q. Lin, ACS Nano 4 (2010) 3053—3062.

[122] L.S. Slaughter, W.-S. Chang, P. Swanglap, A. Tcherniak, B.P. Khanal, E.R. Zubarev, et al., J. Phys. Chem. C 114 (2010) 4934—4938.
[123] C. Novo, A. Funston, I. Pastoriza-Santos, L. Liz-Marzn, P. Mulvaney, Angew. Chem. Int. Ed. 119 (2007) 3587—3590.
[124] K.H. Fung, C.T. Chan, Opt. Commun. 281 (2008) 855—864.
[125] N. Harris, M.D. Arnold, M.G. Blaber, M.J. Ford, J. Phys. Chem. C 113 (2009) 2784—2791.
[126] D.S. Citrin, Nano Lett. 5 (2005) 985—989.
[127] L.A. Sweatlock, S.A. Maier, H.A. Atwater, J.J. Penninkhof, A. Polman, Phys. Rev. B 71 (2005) 7.
[128] F.J.G. de Abajo, A. Howie, Phys. Rev. Lett. 80 (1998) 5180—5183.
[129] F.J.G. de Abajo, A. Howie, Phys. Rev. B 65 (2002) 17.
[130] B. Yan, S.V. Boriskina, B.M. Reinhard, J. Phys. Chem. C 115 (2011) 4578—4583.
[131] L. Chuntonov, G. Haran, Nano Lett. 11 (2011) 2440—2445.
[132] L. Chuntonov, G. Haran, J. Phys. Chem. C 115 (2011) 19488—19495.
[133] J.A. Fan, K. Bao, C.H. Wu, J.M. Bao, R. Bardhan, N.J. Halas, et al., Nano Lett. 10 (2010) 4680—4685.
[134] J. Alegret, T. Rindzevicius, T. Pakizeh, Y. Alaverdyan, L. Gunnarsson, M. Kall, J. Phys. Chem. C 112 (2008) 14313—14317.
[135] S.A. Claridge, S.L. Goh, J.M.J. Frechet, S.C. Williams, C.M. Micheel, A.P. Alivisatos, Chem. Mater. 17 (2005) 1628—1635.
[136] D.L. Jeanmaire, R.P. Vanduyne, J. Electroanal. Chem. 84 (1977) 1—20.
[137] D.W. Brandl, N.A. Mirin, P. Nordlander, J. Phys. Chem. B 110 (2006) 12302—12310.
[138] J.A. Fan, C. Wu, K. Bao, J. Bao, R. Bardhan, N.J. Halas, et al., Science 328 (2010) 1135—1138.
[139] K.C. Vernon, A.M. Funston, C. Novo, D.E. Gomez, P. Mulvaney, T.J. Davis, Nano Lett. 10 (2010) 2080—2086.
[140] M.W. Knight, Y.P. Wu, J.B. Lassiter, P. Nordlander, N.J. Halas, Nano Lett. 9 (2009) 2188—2192.
[141] S.N. Sheikholeslami, A. GarciÃˇAĂĚa-Etxarri, J.A. Dionne, Nano Lett. 11 (2011) 3927—3934.
[142] R.W. Johnson, P.B. Christy, Phys. Rev. B 6 (1972) 4370—4379.
[143] Y.A. Urzhumov, G. Shvets, J. Fan, F. Capasso, D. Brandl, P. Nordlander, Opt. Express 15 (2007) 14129—14145.
[144] S.J. Barrow, X. Wei, J.S. Baldauf, A.M. Funston, P. Mulvaney, Nat. Commun. 3 (2012) 1275.
[145] S.A. Maier, M.L. Brongersma, P.G. Kik, S. Meltzer, A.A.G. Requicha, H.A. Atwater, Adv. Mater. 13 (2001) 1501—1505.
[146] S.A. Maier, P.G. Kik, H.A. Atwater, S. Meltzer, E. Harel, B.E. Koel, et al., Nat. Mater. 2 (2003) 229—232.
[147] H.-Y. Chen, C.-L. He, C.-Y. Wang, M.-H. Lin, D. Mitsui, M. Eguchi, et al., ACS Nano 5 (2011) 8223—8229.
[148] S. Gwo, M.-H. Lin, C.-L. He, H.-Y. Chen, T. Teranishi, Langmuir 28 (2012) 8902—8908.
[149] A.M. Hung, C.M. Micheel, L.D. Bozano, L.W. Osterbur, G.M. Wallraff, J.N. Cha, Nat. Nano 5 (2010) 121—126.
[150] K.E. Korte, S.E. Skrabalak, Y. Xia, J. Mater. Chem. 18 (2008) 437—441.
[151] Y. Sun, Y. Xia, Adv. Mater. 14 (2002) 833—837.
[152] Y. Sun, Y. Xia, Science 298 (2002) 2176—2179.
[153] A. Funston, M. Karg, D. Gomez, K.C. Vernon, T. Davis, P. Mulvaney, in preparation (2012).
[154] A.M. Funston, C. Novo, T.J. Davis, P. Mulvaney, Nano Lett. 9 (2009) 1651—1658.
[155] E. Prodan, C. Radloff, N.J. Halas, P. Nordlander, Science 302 (2003) 419—422.
[156] S.J. Oldenburg, R.D. Averitt, S.L. Westcott, N. Halas, J. Chem. Phys. Lett. 288 (1998) 243—247.
[157] M.W. Knight, Y.P. Wu, J.B. Lassiter, P. Nordlander, N.J. Halas, Nano Lett. 9 (2009) 2188—2192.
[158] C. Novo, A.M. Funston, I. Pastoriza-Santos, L.M. Liz-Marzan, P. Mulvaney, J. Phys. Chem. C 112 (2008) 3—7.
[159] K.C. Vernon, A.M. Funston, C. Novo, D.E. Gomez, P. Mulvaney, T.J. Davis, Nano Lett. 10 (2010) 2080—2086.
[160] M. Hentschel, M. Schaferling, T. Weiss, N. Liu, H. Giessen, Nano Lett. 12 (2012) 2542—2547.
[161] W. Yan, L. Xu, C. Xu, W. Ma, H. Kuang, L. Wang, et al., J. Am. Chem. Soc. 134 (2012) 15114—15121.
[162] A. Kuzyk, R. Schreiber, Z. Fan, G. Pardatscher, E.-M. Roller, A. Hogele, et al., Nature 483 (2012) 311—314.
[163] D. Nykypanchuk, M.M. Maye, D. van der Lelie, O. Gang, Nature 451 (2008) 549—552.
[164] H. Xiong, D. van der Lelie, O. Gang, J. Am. Chem. Soc. 130 (2008) 2442—2443.
[165] M.M. Maye, D. Nykypanchuk, M. Cuisinier, D. van der Lelie, O. Gang, Nat. Mater. 8 (2009) 388—391.
[166] A. Hofmann, P. Schmiel, B. Stein, C. Graf, Langmuir 27 (2011) 15165—15175.
[167] X. Xu, N.L. Rosi, Y. Wang, F. Huo, C.A. Mirkin, J. Am. Chem. Soc. 128 (2006) 9286—9287.
[168] H. Xing, Z. Wang, Z. Xu, N.Y. Wong, Y. Xiang, G.L. Liu, et al., ACS Nano 6 (2011) 802—809.
[169] T. Zhang, Y. Dong, Y. Sun, P. Chen, Y. Yang, C. Zhou, et al., Langmuir 28 (2011) 1966—1970.
[170] C.H. Lalander, Y. Zheng, S. Dhuey, S. Cabrini, U. Bach, ACS Nano 4 (2010) 6153—6161.
[171] T.P. Rivera, O. Lecarme, J. Hartmann, R.L. Inglebert, D. Peyrade, Micro Eng. 86 (2009) 1089—1092.
[172] O. Lecarme, T. Pinedo-Rivera, K. Berton, J. Berthier, D. Peyrade, Appl. Phys. Lett. 98 (2011) 3.
[173] T. Pinedo Rivera, O. Lecarme, J. Hartmann, E. Rossitto, K. Berton, D. Peyrade, J. Vac. Sci. Technol. B: Microelectron. Nanomater. Struct. Process Meas. Phenom. 26 (2008) 2513—2519.
[174] J.A. Fan, K. Bao, L. Sun, J. Bao, V.N. Manoharan, P. Nordlander, et al., Nano Lett. 12 (2012) 5318—5324.
[175] W. Cheng, M.J. Campolongo, J.J. Cha, S.J. Tan, C.C. Umbach, D.A. Muller, et al., Nat. Mater. 8 (2009) 519—525.

**Steven Barrow** received his BSc degree in Nanotechnology from the Royal Melbourne Institute of Technology (RMIT). He then joined Prof. Paul Mulvaney's group at the University of Melbourne as a PhD candidate. His research focuses on the synthesis and DNA mediated self-assembly of metallic nanoparticles and the optical properties of self-assembled nanostructures.

**Dr Alison Funston** is a lecturer and Future Fellow in the School of Chemistry at Monash University, Melbourne, Australia. Dr. Funston received her PhD from The University of Melbourne, Australia, in 2002. She worked as a postdoctoral fellow at Brookhaven National Laboratory with Dr. John Miller in the areas of electron transfer and radiation chemistry. She moved to Monash as a lecturer in 2010 and was awarded an ARC Future Fellowship in 2011. Her research focuses on the energy transport and optical properties of well-defined assemblies of nanoparticles, including metal nanocrystals and semiconductor nanocrystals, as well as charge and energy transfer within nanoparticle:organic systems.

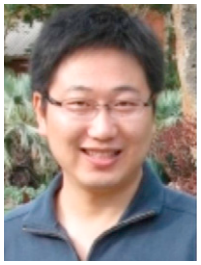

**Xingzhan Wei** received his BS from the University of Electronics Sciences and Technology of China in 2005, and a PhD from Chinese Academy of Sciences in 2010. He is now a postdoctoral fellow with Prof. Paul Mulvaney in the Nanoscience Laboratory at the University of Melbourne. His research interests include modelling, fabrication and characterisation of novel plasmonic structures and metamaterials.

**Paul Mulvaney** is an ARC Laureate Fellow (2011—2015) and Professor of Chemistry at the University of Melbourne. He received his PhD degree from the University of Melbourne in 1989, working on electron transfer kinetics.